The Impact of Forest-Controlled Snow Variability on Late-Season Streamflow Varies by Climatic Region and Forest Structure.

Forest-Snow Variabilities Influence on Late-Season Streamflow in DHSVM

William Ryan Currier[1,2]*, Ning Sun[3], Mark Wigmosta[1,3], Nicoleta Cristea[1], and Jessica D. Lundquist[1]

[1]Department of Civil and Environmental Engineering, University of Washington, Seattle, WA, USA

[2]National Oceanic and Atmospheric Administration, Earth System Research Laboratories, Physical Sciences Laboratory, Boulder, CO, USA

[3]Energy and Environment Directorate, Pacific Northwest National Laboratory, Richland, WA 99352, USA

*Corresponding Author:
National Oceanic and Atmospheric Administration
Earth System Research Laboratories
Physical Science Laboratory
Boulder, CO 80305
Phone: 315-289-2639
Email: william.r.currier@noaa.gov

Index Terms and Keywords

1. Snow
2. DHSVM
3. Forest-snow interactions
4. Summer low streamflow
5. Radiation
6. Silviculture

Abstract

Previous studies have documented how forests influence snow at fine spatial scales, but none have documented the influence that existing forest-snow variability has on streamflow. To test how much forest-controlled snow variability influences streamflow, a tiling parameterization based on classifications from high-resolution (1-3 m) vegetation maps was incorporated into the Distributed Hydrology and Soil Vegetation Model (DHSVM). Within each grid cell (90-150 m), the tiling parameterization simulated forest-snow variability with four independently evolving snowpacks. Each tile had unique radiation conditions to represent conditions underneath the canopy, in exposed areas, and along north- and south-facing forest edges. This tiled parameterization was used to test where and when detailed forest-snow modeling should be considered further and where and when the impacts are too small to be worth the effort. To test this, tiled model simulations of streamflow were compared to non-tiled model simulations in the Sierra Nevada, CA, the Jemez Mountains, NM, and the Eastern Cascades, WA. In Tuolumne, CA, the tiled model simulated little difference in grid cell average SWE, and late-season streamflow decreased by 3-4% compared to the non-tiled model. In Jemez, NM, the tiled model decreased late-season streamflow by 18% due to increased sublimation. In Chiwawa, WA, the tiled model increased late-season streamflow by 15% due to high shortwave radiation attenuation and less longwave radiation enhancement from the forest. Furthermore, within the Chiwawa, a substantial silvicultural practice was synthetically implemented to increase the north-facing edge's fractional area. This silvicultural experiment, which used the same fractional forest area in all simulations increased late-season streamflow by 35% compared to tiled model simulations that did not represent forest edges. In conclusion, representing forest-SWE variability had an effect on late-season streamflow in some watersheds but not in others based on the fractional area of the forest edges, forest characteristics, and climate conditions.

1. Introduction:

Across multiple climates, significant hillslope scale (10 - 100 m) variability in snow depth occurs at forest edges and between exposed and forested areas (Broxton et al., 2015; Clark et al., 2011; Currier & Lundquist, 2018; Hiemstra et al., 2006). Snow depth variability between north- and south-facing forest edges is driven primarily by differences in shortwave and longwave radiation (Golding & Swanson, 1978; Lawler & Link, 2011; Musselman et al., 2008, 2015; Seyednasrollah & Kumar, 2014; Webster et al., 2016, 2017; Woo & Giesbrecht, 2000). Furthermore, snow depth differences between areas directly underneath the canopy and exposed areas are driven by differences in radiation and from subsequent loss after canopy snow interception (Dickerson-Lange et al., 2015, 2017; Lundquist et al., 2013; Mazzotti et al., 2019; Moeser et al., 2016; Storck, 2000; Varhola et al., 2010).

Many spatially distributed hydrologic models implicitly represent forest characteristics and their effect on radiation within a model element. Recent work has suggested the importance of explicitly representing radiation and SWE variability within forests to correctly simulate snowmelt. For instance, prior studies have shown that at coarser spatial scales, models that use bulk canopy metrics and do not account for subgrid snow cover have a different net energy balance and snow melt rate than those at very high resolution (e.g. 1 m) (Broxton et al., 2015; Mazzotti et al., 2020, 2021). Furthermore, previous work, primarily focused on non-forested areas (Brauchli et al., 2017; Luce et al., 1998; Lundquist et al., 2005; Lundquist & Dettinger, 2005; Sexstone et al., 2020; Seyfried & Wilcox, 1995), has shown that improved representation of snow heterogeneity increases modeled late-season streamflow. However, previous studies have not documented how a finer-scale representation of forest-snow interactions impacts basin-

scale streamflow and whether that impact varies across regions with different climates and different forest cover.

Here, we implement a tiling parameterization that was first introduced in Currier and Lundquist (2018) to explicitly represent forest-snow processes and their effect on sub-grid snow variability in the Distributed Hydrology and Soil Vegetation Model (DHSVM) (Wigmosta et al., 1994, 2002) (Section 3). We then test the degree to which this explicit representation changes streamflow in watersheds located in the Sierra Nevada, CA, the Jemez Mountains, NM, and the Eastern Cascades, WA. These sites represent a gradient from dry-sparse-forest to wet-dense-forest. While lidar and streamflow observations were used extensively to ensure the model simulations captured reality (Section 3.d., Section 4.a.ii), our objective was to test the impact of different forest-snow representations within a model on streamflow rather than to achieve a perfectly calibrated model. A driving and fundamental question was where and when such detailed forest-snow modeling should be considered further and where and when the impacts are too small to be worth the effort.

With these goals in mind, we conducted three general experiments. First, within two of the watersheds, Tuolumne, CA, and Jemez, NM, we compared simulated SWE to lidar-derived SWE in each tile to evaluate the model's representation of subgrid variability (Section 4.a.ii.). At these locations, we showed how radiation differences led to subgrid SWE variability (Section 4.a.iii.). In addition, we quantified the effect that the tile parameterization had on grid cell average SWE (Section 4.a.i), evapotranspiration (Section 4.a.i, Section 4.b.), and streamflow (Section 4.b.), compared to the implicit forest parameterization within the original, non-tiled version of DHSVM, which used a single snowpack per grid cell.

Second, we also applied the tiled model to a watershed in the Eastern Cascades of Washington State - the Chiwawa Watershed (Section 4.c.). Similar to the other watersheds, in the Chiwawa, we explored the tiled model's effect on grid cell average SWE and late-season streamflow compared to the non-tiled version of DHSVM. In addition, the Chiwawa was heavily forested, and silvicultural prescriptions are actively being explored in Eastern Washington to decrease wildfire risk, maximize snow retention, and increase late-season streamflow for salmon spawning (Churchill et al., 2013; Haugo et al., 2015; Hessburg et al., 2015; WDNR, 2018; Wigmosta et al., 2015). Motivated by silvicultural interests within the region, DHSVM was recently modified to synthetically introduce forest gaps within the Chiwawa Watershed, which led to an increase in late-season streamflow (Sun et al., 2018). We build off these results in the discussion and synthetically alter the forest to implement east-west oriented clearings (Section 5.c.). Our forest management strategy differed from Sun et al. (2018), and we focused on how the representation of subgrid-SWE variability affects late-season streamflow within the managed forest rather than comparisons between managed and unmanaged forests.

Third, within all three watersheds, and within the silvicultural experiment, we determined the relative importance of representing forest edges (Section 5.b.). To do so, we adapted the tiled model to only represent forest and exposed areas (two snowpacks) and no longer represent forest edges. We then compared streamflow simulations that represented four snowpacks per grid cell (north- and south-facing forest edges, exposed, and forested areas) to simulations that only represented two snowpacks per grid cell (exposed and forested areas).

2. Location and Data

a. Site overviews

We chose three watersheds for our study that differed in forest characteristics, meteorological conditions, and elevation distributions, but had publicly available lidar data (Figure 2; Table 1). Tuolumne, CA was the highest elevation location and contained primarily lodgepole pine (*Pinus contorta*) and generally had the shortest trees. In Tuolumne, CA, we focused on the Upper Tuolumne due to available streamflow observations, where the forest cover was less than half the watershed. In Jemez, NM there were a variety of different tree species such as Douglas fir (*Pseudotsuga menziesii*), white fir (*Abies concolor*), blue spruce (*Picea pungens*), limber pine (*Pinus flexilis*) and ponderosa pine (*Pinus ponderosa*). The trees in the Jemez were less dense than in the Upper Tuolumne and generally more dispersed. Furthermore, Jemez was the driest location and received the highest amounts of incoming shortwave radiation throughout the winter (Table 1). Chiwawa, WA was the wettest location and received the least amount of incoming shortwave radiation. The Chiwawa primarily consisted of grand fir (*Abies grandis*) at low elevations and subalpine firs (*Abies lasiocarpa*) at high elevations. The Chiwawa had the densest and tallest canopy, with the greatest spatial coverage in forests (Table 1).

b. Model Input Data

In Tuolumne, maps describing the vegetation were provided from lidar data (Painter et al., 2016), and the National Land Cover Database's (NLCD) classifications (Homer et al., 2015) (Section 2d). Model runs were conducted at a 150-m spatial resolution and a one-hour timestep for water year (WY) 2016 as this was a normal SWE year.

In the Jemez and Chiwawa, maps describing the vegetation classification were provided from lidar data (Department of Natural Resources, 2020; Harpold et al., 2014), imagery from the National Agriculture Imagery Program (NAIP), and NLCD landcover classifications (Section 2d). In the Jemez, model runs were conducted at a 150-m spatial resolution and a one-hour timestep for WY 2010 due to the snow-on lidar date. In the Chiwawa, model input data and configurations were consistent with Sun et al. (2018), except for the vegetation maps to make the results transferrable. Model runs were conducted for WY 2011 at a 90-m spatial resolution and a one-hour timestep to be consistent with Sun et al. (2018).

Lastly, DHSVM forcing data is described in Text S1 for brevity within the main text.

c. Measured Snow Depth and Streamflow

Distributed snow depth data were derived from lidar data in the Upper Tuolumne at 3-m spatial resolution (Painter et al., 2016), and for a subset of the Jemez River Watershed at 1-m spatial resolution (Harpold et al., 2014) (Figure 2). Lidar-derived snow depth data were not available for the Chiwawa Basin. Lidar-derived snow depth generally has errors less than 10-cm (Painter et al., 2016) and the errors in the forest were comparable to errors in exposed areas (Currier et al., 2019; Mazzotti et al., 2019). DHSVM simulated SWE, and therefore, snow density was derived using methods in Sturm et al. (2010) in combination with Sturm et al. (1995), based on which the lidar-derived snow depth was converted to SWE. Additional SWE observations exist at snow pillows in all three basins (Figure 2). Snow pillows were used for model calibration in exposed regions (Section 3d). USGS stream gage data were provided from the Jemez River Near Jemez, NM (USGS 08324000) and the Chiwawa River Near Plain, WA (USGS 12456500) gages. Streamflow data in the Upper Tuolumne were provided from the

network described in Lundquist et al. (2016), where we focused on the Highway 120 gage (Figure 2, top panel).

d. Vegetation maps

Lidar derived canopy height maps were used to classify canopy grid cells at a 1-3 m spatial resolution. However, in the Jemez and Chiwawa watersheds, 1-m gridded lidar data were only available over a subset of the watershed (Figure 2). In areas where lidar data were not available, canopy grid cells were identified using the Normalized Difference Vegetation Index (NDVI) from 4-band NAIP imagery at 1-m spatial resolution (Figure 3). Canopy grid cells were identified when the NDVI was greater than a threshold value. The threshold value was determined based on the greatest agreement between the lidar-derived canopy mask and the NDVI derived canopy mask (Figure 3) resulting in NDVI thresholds of 0.27 and 0.02 in the Jemez and Chiwawa, respectively. Differences in NDVI thresholds were likely due to a combination of differences in species type (Section 1a), plant health, the forest understory, and the amount of mosses and twigs within the trees (Huemmrich & Goward, 1997; Xiao & McPherson, 2005).

NDVI- and lidar-derived canopy masks were classified into north- and south-facing edges using methods described in Currier and Lundquist (2018). The classification algorithm searched out a specified distance directly north and south from a classified forest grid cell, which was classified based on a lidar derived canopy height map (>2 m) or the previously described NDVI method. If the classified grid cell was not a forest grid cell and was within the search distance, the grid cell was classified as either a north- or south-facing forest edge. Where north- and south-facing forest edges overlapped, we classified the grid cell as an exposed area based on visual inspection of lidar-derived snow depth data. Overlapping areas showed both relatively low snow

depths on the south side of the trees and areas of higher snow depth on the north side. Therefore, on average, overlapping areas showed values closer to what was represented in exposed areas.

Search distances were based on tree height. Where canopy height data were not available (NDVI classification), the average tree height from the lidar domain was used. Forest-edge search distances were two-tree heights to the north and 3 m to the south. Currier and Lundquist (2018) showed that statistically significant snow depth differences existed between north- and south-facing edges when the search distance was two-tree heights for the Jemez and Upper Tuolumne. In contrast to Currier and Lundquist (2018), we specified the south-facing forest edge as 3 m because enhanced longwave radiation (from the south-facing side of the tree receiving more solar radiation) has a length scale of around 3 m, irrespective of tree height (Musselman & Pomeroy, 2017).

The high-resolution classification maps (1-3 m) were aggregated to the model resolution (90-150 m) to create four unique, fractional area maps. Each map represented the grid cell's fractional area that was exposed, forested, or was a part of a north- and south-facing edge. The sum of all four maps was equal to one.

After aggregation to 90-150 m grid cells, the fractional vegetation maps and associated vegetation classifications used within DHSVM (NLCD 2011 vegetation classifications) were adjusted. For instance, identifying canopy grid cells from NAIP imagery was particularly problematic in riparian areas or alpine areas that were noticeably green after snow melt. These areas had high NDVI values but did not contain vegetation greater than 2 m (Figure 3). To filter out erroneous fractional vegetation areas the NLCD 2011 vegetation classifications were used. If the NLCD 2011 map was not a deciduous, evergreen, or mixed forest, but the NAIP imagery classified part of the grid cell as forested, the fractional area for the exposed map was set equal to

one (fractional forest, north, and south-facing maps were equal to zero). Lastly, after filtering with the NLCD 2011 map, if the fractional forest area was greater than zero, the vegetation classification used within DHSVM was relabeled an evergreen forest for simplicity.

3. Methods

a. Model Description

DHSVM (version 3.2) is a process-based, spatially distributed model that explicitly solves the water and energy balance at grid cell scales of 30-150 m. DHSVM simulated the physical processes that govern surface and subsurface runoff generation, such as canopy interception, evapotranspiration, snow accumulation and melt, and soil water dynamics (Wigmosta et al., 1994, 2002). DHSVM simulated SWE at the ground surface within a grid using a two-layer energy and mass balance snow model (Wigmosta et al., 1994, 2002). It explicitly accounted for the influence of topography and vegetation cover on snowpack dynamics. In grid cells with a canopy, DHSVM also simulated canopy snow interception, sublimation, mass release, and melt with a one-layer mass-and energy balance canopy model (Storck, 2000; 2002; Wigmosta et al., 1994, 2002). Wind speeds in forested grid cells were scaled from the reference height to two meters using an exponential profile, while wind speeds in grid cells that were in exposed areas were scaled using a logarithmic profile (Andreadis et al., 2009; Storck, 2000). The evapotranspiration rate was calculated using a Penman-Monteith approach (Monteith, 1965; Wigmosta et al., 1994), and DHSVM allowed surface and saturated subsurface flow to be transported to neighboring grid cells. For more details see Wigmosta et al., (1994, 2002).

b. Radiation Balance

i. Non-tiled Model

In the non-tiled framework of DHSVM, there was a single snowpack that evolved per grid cell. Net shortwave radiation at the snow/soil surface (understory) for a grid cell with an overstory was calculated as follows:

$$SW_{net}^{under} = (1-\alpha) * \left(SW_{in}\,(1-F) + F\left(SW_{dir}\tau + SW_{diff}\tau_d\right)\right) \quad (1)$$

where incoming shortwave radiation (SW_{in}) was partitioned into direct and diffuse components, SW_{dir} and SW_{diff}, respectively. The radiation partitioning was based on regression coefficients and a ratio between the incoming atmospheric shortwave radiation and the solar constant. *F* is the fractional forest cover parameter, which varied spatially using methods discussed in section 2d (Figure 2). α, is the albedo for either the snowpack or understory vegetation, depending on whether snow was present. τ is the canopy transmittance coefficient for direct radiation, and τ_d is the overstory's transmittance coefficient for diffuse radiation. τ_d is a input parameter that varied based on vegetation type, while τ was calculated based on tree height (*H*), the sun's elevation angle (*el*), and an extinction coefficient (*k*). *k* is an input parameter which varied monthly and by vegetation type.

$$\tau = exp\left(\frac{-k*H}{sin\,(el)}\right) \quad (2)$$

Outgoing and incoming longwave radiation for a grid cell with a canopy was calculated for the understory or ground snowpack as follows:

$$L_{out}^{under} = \sigma {T_{srf}}^4 \quad (3)$$

$$L_{in}^{under} = L_d(1-Vf) + \sigma {T_{can}}^4 F \quad (4)$$

where L_d, is the incoming atmospheric longwave radiation, σ is the Stefan-Boltzmann constant, T_{can} is the canopy temperature, which was equal to the air temperature, T_{srf}, is the snow or soil temperature, and Vf is F multiplied by a tunable canopy view adjustment factor (Thyer et al., 2004). The canopy view adjustment factor accounted for canopy gaps within the grid cell from the spacing of individual trees, or air space within the tree itself due to the spacing of the branches and needles or leaves. In the case where there is no overstory, the incoming longwave for the understory is L_d.

Net radiation was calculated as:

$$Net\ Rad = SW_{net}^{under} + L_{in}^{under} - L_{out}^{under} \quad (5)$$

Therefore, for a grid cell that had a canopy, radiation variability within a DHSVM grid cell was a weighted average between radiation in an exposed area and radiation underneath the forest, where the weights per grid cell were based on the fractional forest cover parameter, F. Note that snow albedo, which was a function of snow surface temperature and the days since snowfall, was not a weighted average based on F, as there is a single snowpack that evolves per grid cell.

ii. Tiled model

Within the tiled model, there are up to four snowpacks per grid cell, each tile evolved with a different albedo, snow surface temperature, and pack temperature. Net shortwave radiation for each tile was modeled as follows (Figure 4) and equations 6-9 are organized from the tile that received the least amount of net shortwave radiation to the most amount of net shortwave radiation.

$$SW_{net}^{Forest} = (1 - \alpha^{Forest}) * \left(SW_{dir}\tau + SW_{diff}\tau_d\right) \quad (6)$$

$$SW_{net}^{nf} = (1 - \alpha^{nf}) * \left(SW_{dir}\tau_{dir,nf} + SW_{diff}\tau_{nf}\right) \quad (7)$$

$$SW_{net}^{sf} = (1 - \alpha^{sf}) * \left(SW_{dir} + SW_{diff}\tau_{sf}\right) \quad (8)$$

$$SW_{net}^{Exposed} = (1 - \alpha^{Exposed}) * \left(SW_{dir} + SW_{diff}\right) \quad (9)$$

τ_{nf} and τ_{sf} are model input parameters, which were both set to 0.75 in this study to represent that 75% of the diffuse radiation was incident at the snow/soil surface. Within the forest tile and in the non-tiled model τ_d was set to 0.215 as more diffuse radiation is attenuated underneath the canopy than at the edge. Direct radiation attenuation at the northern edge was similar to the forest (Equation 6) but we introduce, $\tau_{dir,nf}$, which was the direct radiation transmittance at the north-facing edge, to allow for more direct shortwave radiation at the north-facing edge than directly underneath the forest. $\tau_{dir,nf}$ was calculated as the product of $\tau_{dir,nf} = \tau + \tau * \tau_{mult}$, where τ_{mult} is a user defined multiplicative scalar. $\tau_{dir,nf}$ was capped at 1.0 and does not vary with time of year for simplicity. Net shortwave radiation for the forest (Equation 6) and exposed areas (Equation 9) were based on the forest and exposed components from equation 1 (Figure 4). Net shortwave radiation at the south-facing edge received direct solar radiation that was not attenuated (Figure 4), but 25% of the diffuse radiation was attenuated by the forest due to the reduced sky view from the forest to the north.

Outgoing longwave radiation had a similar form to equation (3) for all tile components. Incoming longwave radiation for the forest and exposed regions was modeled identical to equation (4), where *F* was equal to 1 for the forest tile, and in the exposed tile *F* was equal 0. Incoming longwave radiation at north- and south-facing forest edges was calculated similar to equations 3-4, but instead *F* was replaced by additional input parameters, F_{nf} and F_{sf}. F_{nf} and F_{sf} weight the magnitude to which the forest edge receives longwave radiation from the forest and the atmosphere.

$$L_{in}^{nf} = L_d(1 - F_{nf}) + \sigma {T_{can}}^4 F_{nf} \quad (10)$$

$$L_{in}^{sf} = L_d(1 - F_{sf}) + \sigma {T_{can}}^4 F_{sf} \quad (11)$$

F_{nf} and F_{sf} were user supplied. Note that F_{nf} and F_{sf} are not the same as the grid cell's fractional area for north- and south-facing areas but rather are used to control how much longwave radiation is incident on the north- and south-facing snowpacks, respectively.

In the forest tile's longwave calculation, F is set to one and then scaled by the canopy view adjustment factor to represent air space within the canopy (section 3.b.i.). Therefore, for a tiled model that only contains exposed and forest tiles, the grid cell average incoming shortwave radiation and longwave radiation is the same as the non-tiled model. However, the net shortwave radiation and longwave radiation are not the same as the non-tiled model because the different amounts of radiation incident on the two snowpacks lead to each tile evolving with a different albedo, snow surface temperature, and pack temperature.

Model parameters, F_{nf}, F_{sf}, and τ_{mult} were adjusted in Jemez and Tuolumne independently so that simulations from the calibrated model would match the mean of the lidar-derived SWE for each tile's classification within the grid cell (Table 2). For instance, using the high-resolution classification within a grid cell (Section 2d), we calculated the mean of the lidar-derived SWE observations for the north-facing edge to compare with the simulated north-facing SWE at a particular grid cell. In Tuolumne, we used multiple lidar flights to look at observed and simulated SWE throughout the ablation season and near peak SWE. In the Chiwawa, we use model parameters from both Tuolumne and Jemez, as lidar-derived SWE observations in the Chiwawa were not available (Table 2).

For tiled grid cells, the north-facing, south-facing, and exposed tiles had wind speeds and the aerodynamic resistance (before a stability correction) scaled based on a weighted average

between winds experienced in the open and under the continuous canopy. We set the weight equal to the forest's fractional area per grid cell, which was determined from the lidar and NAIP data, similar to Sun et al. (2018). The tiling parameterization did not account for wind direction and therefore did not explicitly account for wind sheltering. Furthermore, snow processes related to snow transport or preferential deposition were not accounted for within DHSVM, although we acknowledge that these processes are often important to represent (Brandle, J.R., Finch, 1991; Hiemstra et al., 2002, 2006; Luce et al., 1998; Webb et al., 2020).

c. Mass Balance

In the tiled model, the forest tile was the only tile where canopy snow interception was simulated. Canopy snow interception for the forest tile was consistent with the original DHSVM framework and is described in Storck (2000) and Wigmosta et al. (1994). In the tiled model, the *F* parameter was again set to one to ensure that the tiled model had the same fraction of precipitation intercepted throughout the grid cell as the non-tiled model.

Each tile simulated evapotranspiration, using a Penman-Monteith approach when snow was absent in the tile except for the forest tile (Monteith, 1965; Wigmosta et al., 1994, 2002). The forest tile allowed for evapotranspiration from the overstory while snow was present in the understory. Total evapotranspiration includes soil evaporation, transpiration, and canopy evaporation. Since each tile evolved its own independent snowpack, each tile melted out at a different time, therefore evapotranspiration began at different times for each tile. Each tile's flux of evapotranspiration, sublimation, snowmelt, and soil moisture were aggregated based on a weighted average that used each tile's fractional area as a weight. Grid cell average snowmelt was added to total surface water input, which infiltrated into the grid cell average soil reservoir using methods described in Wigmosta et al. (1994). At the start of the next time step, each layer

of each tile's soil moisture reservoir was reset based on the grid-cell average soil moisture for each soil layer, assuming that lateral fluxes caused this to equilibrate quickly within the 90-150 m grid cell.

d. Model Calibration and Baseline Simulations

The original, non-tiled version of DHSVM was manually calibrated at the three sites to provide reasonable simulations of SWE and streamflow for three water years. Therefore, model calibration refers to adjusting parameters within the non-tiled version of DHSVM and does not reference any adjustments of parameters that are specific to the tiled model (Section 3b.ii.). DHSVM was first calibrated to simulate SWE at snow pillow locations within the basin (Figure 2; Figure 5). Afterwards, the model was manually calibrated against streamflow observations using the Nash Sutcliffe's Efficiency (NSE) metric (Figure 5). More details on model parameter decisions and differences amongst model parameters between basins are provided in the supplemental material (Cristea et al., 2014; Cuo et al., 2011; Daly et al., 2008; Dingman, 2002; Du et al., 2014; Homer et al., 2015; Meyer et al., 1997; Small & McConnell, 2008; Storck, 2000; Sun et al., 2018; Thyer et al., 2004; Wigmosta et al., 1994; Zhao et al., 2009). All non-forest parameters were held constant between the tiled and non-tiled runs.

4. Results

a. Single Grid Cell: SWE and Energy Balance Evaluation at Tuolumne and Jemez

i. Tiled Model vs. Non-Tiled Model: Grid Cell Average SWE

Simulated grid cell average SWE in Tuolumne and Jemez led to similar snow disappearance dates between the tiled and non-tiled model (Figure 6a,b black solid vs. gray dashed lines). At

the Tuolumne evaluation site, Dana Meadows South, the tiled model had a snow disappearance date 1 day later than the non-tiled model (Table 3). Similarly, at the evaluation site in Jemez, NM, the tiled model had the same snow disappearance date as the non-tiled model. Furthermore, the tiled and non-tiled model simulated similar peak SWE values (Table 3).

ii. Tiled Model: Subgrid SWE Comparisons to Observations

At both Tuolumne and Jemez, the tiled model simulated reasonable SWE variability compared to the observed variability within the grid cell from the lidar observations (Figure 6a,b). For instance, the rank order of the lidar-derived SWE observations matched the rank order of simulated SWE in each tile. At both locations, the north-facing edge accumulated the most SWE, while the forest tile simulated the least amount of SWE at peak (Table 3). South-facing edges accumulated more SWE than the forest tile, but in both locations, south-facing edges melted faster than the forest tile. In Tuolumne, the south-facing edge melted out 20 days before the tiled model's grid cell average and 19 days before the north-facing edge. The slowest melt rate in Tuolumne occurred in the forest, and therefore snow disappeared from the forest last, which was consistent with the lidar observations (Table 3). At Jemez, the slowest melt rates also occurred in the forest. This slow melt rate led to a melt out date 4 days later than in exposed areas, which was consistent with previous findings (Harpold et al., 2015; Molotch et al., 2009). Furthermore, in Jemez, the south-facing edge melted out 30 days earlier than the north-facing edge, with snow disappearing from the north-facing edges last, which was also consistent with previous work (Musselman et al., 2008).

iii. Tiled Model: Radiation Conditions Drove Subgrid SWE Variability

Subgrid SWE variability amongst north-facing, south-facing, and exposed tiles was driven by differences in net shortwave radiation, incoming longwave radiation, and differences between each tile's snow surface temperature (Figure 6). For instance, within the north-facing, south-facing, and exposed tiles, the rank order in net radiation during daylight hours was inversely related to the snow disappearance dates (Figure 6i,j). The forest tile accumulated less SWE, due to forest-snow interception and subsequent loss, but contained relatively slower melt rates due to lower amounts of incoming shortwave radiation from canopy shading. At both locations, the forest tile had the lowest amount of net shortwave radiation followed by the north-facing edge (Figure 6c,d). Tuolumne's north-facing edge experienced relatively higher net shortwave radiation than Jemez because Tuolumne had a higher τ_{mult} , which resulted from tuning the model parameter to match the observed SWE distribution (Table 2). At both locations, the south-facing edge tile experienced slightly less net shortwave radiation than exposed regions due to the attenuation of diffuse radiation. The incoming longwave radiation at the north- and south-facing forest edges were similar due to similar F_{sf} and F_{nf} values (Table 2, Figure 6e,f).

iv. Single Grid Cell: Hydrologic Fluxes at Tuolumne, CA and Jemez, NM

In Tuolumne, grid cell average hydrologic fluxes were similar between the tiled and non-tiled model (Figure 7a). For instance, the tiled model simulated similar amounts of total snowmelt, evapotranspiration, sublimation, saturated flow, and infiltration excess flow. Furthermore, temporal changes in soil moisture were similar between the two models. The tiled model's soil moisture content increased earlier due to the south-facing edge melting out sooner than the non-tiled model. Furthermore, there were subtle differences in the soil moisture drawdown rates due to slight increases in the tiled model's evapotranspiration rates after the snow disappeared.

However, these differences were relatively small and therefore in Tuolumne, there were no notable differences between the tiled and non-tiled model.

At Jemez, NM's evaluation site, the tiled model simulated 21.2 mm (7%) less snow melt than the non-tiled model (Figure 7b). Less total snowmelt was primarily driven by differences in sublimation. The tiled model simulated more total sublimation than the non-tiled model by 15.7 mm (Figure 7e,f). While tiles showed increased sublimation, the reason for the tiled model's increased sublimation rates was different for the forest tile than the other tiles. For instance, the exposed, north-, and south-facing edge tiles had higher relative wind speeds compared to the forest tile and the non-tiled model based on different scaling of the wind speed from the reference height. The forest tile and the non-tiled model contained the same wind speeds (Section 3b). However, within the forest tile, the surface temperatures were sometimes greater than the air temperature in the evening (Figure 6h) due to relatively high amounts of incoming longwave radiation (higher than in the non-tiled model, Figure 6f) that kept the snow surface warm. Relatively warm snow surface temperatures at night led to unstable conditions and a relatively low aerodynamic resistance value. Therefore, the forest tile had the same wind speeds as the non-tiled model, but the relatively warm snow surface temperatures within the forest tile resulted in higher sublimation rates than the non-tiled model. This hillslope scale spatial variability in sublimation exhibited by the tiled model (Figure 7f), due to differences in wind speed, shortwave radiation, and enhanced longwave radiation from the forest, was previously shown with observations by Musselman et al. (2008). In addition, the rank orders of sublimation (Figure 7f) from the tiled model simulations were consistent with high resolution, 1-m SnowPALM simulations grouped by under canopy, near canopy, and distant canopy pixels (Broxton et al., 2015).

b. Effects on Streamflow in Tuolumne, CA and Jemez, NM

In Tuolumne, the tiled model increased the variability in SWE within all forested grid cells throughout the watershed, but there was little effect on late-season streamflow. In Tuolumne, the tiled model produced a 1-2% increase in streamflow between April and June and a 3-4% decrease in streamflow after mid-June (Figure 8). In net, the tiled model simulated 0.4% less total annual streamflow volume than the non-tiled model. In Tuolumne, north-facing edges represented 4% of the watershed, and 45% of the grid cells were forested (Table 1). This relatively small forest and forest edge representation, combined with similar melt out dates between exposed, forest, and north-facing tiles explained the small effect on streamflow in Tuolumne. Therefore in Tuolumne, it was not critical to represent subgrid forest-SWE variability in order to accurately represent streamflow

In Jemez, north-facing edges represented 20% of the watershed and 80% of the 150-m grid cells were at least partly forested. Streamflow in May-June (before the monsoon season) from the tiled model was about 18% less than the streamflow from the non-tiled model (Figure 8). In net, the tiled model simulated 8% less total streamflow than the non-tiled model. At both locations, aggregated basin-wide total evapotranspiration was nearly identical between the tiled model and the non-tiled model (Figure 8a b), suggesting that the difference in simulated streamflow in Jemez, NM between the tiled and non-tiled model was primarily due to differences in sublimation (Figure 7f).

c. Chiwawa Watershed

The Chiwawa Watershed contained no observations of SWE in the forest to evaluate individual tile parameters within DHSVM, as the Eastern Cascades represent a gap in forest-snow observations (Dickerson-Lange et al., 2021). However, the Chiwawa Watershed was

chosen because the watershed is heavily forested, it is located within the Eastern Cascades where there is significant interest in silvicultural practices that decrease wildfire risk, restore ecological health, and increase late-season streamflow to maintain salmonid habitat requirements (Churchill et al., 2013; Haugo et al., 2015; Hessburg et al., 2015; WDNR, 2018; Wigmosta et al., 2015).

At the Chiwawa, WA evaluation site, both the Tuolumne and Jemez parameters (Table 2) produced substantial variability in SWE (Figure 9a,b). The tiled model's grid cell average SWE melted out 36 and 28 days later than the non-tiled model using the Tuolumne and Jemez parameters, respectively. This was due to the relatively tall trees (Table 1), which led to relatively high attenuation of direct beam solar radiation (Equation 2). This resulted in relatively slow melt rates within the forest tile, and the north-facing edge accumulated SWE throughout May while the south-facing and exposed tiles were melting. The tiled model simulations in the Chiwawa showed that snow lasted substantially longer in the forest than in the open. This finding was consistent with the predicted climate-forest-snow classes from Dickerson-Lange et al. (2021). Furthermore, this was consistent with the framework proposed by Lundquist et al. (2013), who showed that locations with relatively cold mean winter temperatures have greater snow retention in the forest from relatively less forest-snow interception and less enhanced longwave radiation from the forest.

In the Chiwawa, despite similar looking hydrographs, the tiled model led to a 15% increase in August and September streamflow values (Figure 9c,d). This was driven primarily by the forest tiles' slow melt rate, as north-facing forest edges were only 2% of the watershed (Table 1). The tiled model's annual evapotranspiration amounts were 19 mm (2.5%) less than the non-tiled model. Furthermore, total sublimation amounts in the tiled model were 1 mm higher than the non-tiled model, and total sublimation rates were low (<1% of peak SWE) in both the tiled and

non-tiled model. Relatively small differences in evapotranspiration and sublimation between the tiled and non-tiled model suggested the increase in late-season streamflow in Chiwawa, WA was primarily due to a more detailed representation of subgrid radiation variability in forested and exposed areas.

5. Discussion

a. Existing forest characteristics and climate conditions effect on streamflow

The explicit representation of subgrid forest-SWE variability affected late-season streamflow differently based on the forest characteristics and climate conditions. In the Jemez River Watershed, which had a relatively sparse forest and a relatively warm, sunny, and arid climate, the more explicit representation of the forest led to an increase in sublimation (Section 4.a.iv., Figure 7), which decreased simulated streamflow (Section 4.b., Figure 8). This increase in sublimation following the more explicit forest representation was consistent with observations and modeling studies in the literature. For instance, Broxton et al. (2015) and Musselman et al. (2008) showed spatial variability in sublimation rates. Biederman et al. (2014) and Harpold et al. (2014) showed that increases in solar radiation following canopy removal led to an increase in sublimation. While the tiled model did not change the fractional forest area in the Jemez, each tile had differences in the radiation budget compared to the non-tiled model, which led to an increase in total sublimation.

In the Chiwawa River Watershed, which had a dense canopy with significant shortwave radiation attenuation and a relatively cold and wet climate (Table 1), the explicit representation of radiation conditions underneath the forest increased late-season streamflow (Section 4.c., Figure 9). In the Chiwawa, relatively cold air temperatures led to less longwave radiation

enhancement from the forest than there was in Tuolumne or Jemez. Furthermore, the relatively tall trees led to more shortwave radiation attenuation, which led to later melt out dates directly underneath the forest and an increase in late-season streamflow. While there is a data gap in forest-snow observations within the Eastern Cascades, or locations with similar temperatures and precipitation magnitudes, the rank order of melt out dates agreed with conceptual models and our understanding of the physical processes (Dickerson-Lange et al., 2021; Lundquist et al., 2013). In the Tuolumne River Watershed, which had less shortwave radiation attenuation from the forest than the Chiwawa and is not as warm and dry as the Jemez, the explicit representation of forest-snow variability did not have a significant impact on grid cell average snowmelt and thus streamflow (Figure 7,8).

b. Forest Edge Effects on Streamflow

To compare the effect that simulating forest edges to the effect of simulating separate below-forest vs open snowpacks for each grid cell, the tiled model was run with the north- and south-facing fractional areas converted to exposed areas. Therefore, the forest edges were removed from the tiled model, and the tiled model only simulated forest and exposed tiles. In Tuolumne there were nearly identical simulations between tiled model simulations that contained and did not contain forest edges, both of which did not have a notable difference in streamflow from the non-tiled model. In Jemez, the tiled model without forest edges decreased May-June streamflow by 20%, while the simulations with forest edges decreased May-June streamflow by 18%, relative to the non-tiled model. In Chiwawa, August-September streamflow increased 12% when forest edges were not accounted for. Meanwhile, the tiled model with forest edges increased streamflow by 15%. Therefore, within these three watersheds, representing forest edges did not notably affect streamflow simulations. Instead, it was more important to separately evolve the

snowpack in exposed and forest tiles. Forest edges either represented a relatively small fractional area within the watershed (Tuolumne and Chiwawa), or the forest edges had similar melt out dates and had higher sublimation rates (Jemez).

c. Chiwawa Watershed: A synthetic forest management benchmark

Here we used the tiled model to benchmark the extent to which north-facing forest edges influence late-season streamflow by synthetically implementing a substantial forest management plan within the tiled model. To understand the influence that north-facing edges could have on streamflow in the Chiwawa Watershed of Washington State, we introduced east-west forest clearings wherever there were evergreen forest grid cells (Figure 10a). East-west forest clearings were introduced throughout the entire forest by adjusting the fractional area maps for each tile. Forest strips were designed to maximize the north-facing forest edge representation within a 90-m grid cell. For instance, within the 90-m DHSVM grid cell, 40% of the grid cell was a forest, 30% was a north-facing edge, which is around two-tree heights, 26% was an exposed tile, and 4% was a south-facing edge, which is consistent with the extent of enhanced longwave radiation from the forest (Figure 10a). The tiled model with four snowpacks per grid cell was compared to the tiled model without forest edges (two snowpacks per grid cell), as done in section 5b.

The tiled model that represented forest edges with the synthetically managed forest in the Chiwawa Watershed increased July streamflow by 30-33%, August streamflow by 42-43%, and September streamflow by 30-34% relative to the tiled model configuration that only represented forested and exposed tiles (Figure 10c). Ranges were based on using the forest-edge parameters from Tuolumne, CA or Jemez, NM (Table 2). In net, the tiled model resulted in a 1% higher total annual streamflow volume than the tiled model without forest edges. Therefore, north-facing

forest edges within certain climates and forest configurations have the potential to substantially increase late-season streamflow.

A similar forest management strategy was tested in the Tuolumne and Jemez. In Tuolumne, maximizing north-facing forest edges did not alter late-season streamflow due to similar melt out dates between north-facing, forest, and exposed tiles as well as much of the streamflow volume coming from the alpine region, which contributes a substantial amount of the late-season streamflow. In Jemez, we found that north-facing edges within the synthetically managed forest were able to substantially increase late-season streamflow but only for a two week period in late May and early June (see supplemental material). While in the Chiwawa we saw an increase in streamflow that was sustained over several months of the dry season (July – September). We note that implementing east-west clearings in the Jemez would likely be more difficult than in the Chiwawa due to a more dispersed spacing of individual trees whereas in the Chiwawa the forest was much denser.

Lastly, results from the synthetic forest management benchmark were different than previous forest management studies. Specifically, Sun et al. (2018), who converted 24% of the Chiwawa watershed to 60-m diameter gaps and found an increase in late-season streamflow by about 20% compared to the non-managed forest. Our results focused on comparing the same two forest structures but with a different level of model detail.

d. Future work

Future work could use the tiled model for more targeted forest restoration practices, specifically focusing on certain slope and aspects. Additionally, the model users could consider altering areas based on land ownership, wilderness area restrictions, riparian areas, and areas where the slopes are too steep. Furthermore, future work should focus on using the tiled model

for forest restoration practices that return the landscape to be more consistent with a natural fire-dominated condition, which introduces a more heterogeneous spatial distribution (forest gaps and clumps of trees), rather than east-west forest strips.

In all watersheds, forest edges did not significantly influence streamflow when tiled model simulations used the existing forest structure (Section 5.b.). However, forest edges were particularly important in the Chiwawa when the forest was significantly managed to increase the fractional area of north-facing edges (Section 5.c., Figure 10). Due the significant response in streamflow within the Chiwawa, additional radiation observations and/or SWE observations at the forest edge, and in areas directly underneath the canopy could help constrain and validate model parameters in Table 2 for the Chiwawa, or similar Eastern Cascade watersheds where there is a data gap (Dickerson-Lange et al., 2021).

6. Conclusions

Impacts of representing forest-snow heterogeneity varied dramatically across different regions. In Tuolumne representing subgrid forest-SWE variability did not significantly affect streamflow, due to similar snow date disappearances between forest and exposed tiles, and a relatively small fractional forest area within the watershed. In Jemez, where north-facing forest edges represented 20% of the watershed's forested grid cells, the tiled model resulted in a higher percentage of the snowpack lost to sublimation. The increase in sublimation decreased late-season streamflow and annual streamflow volumes relative to the non-tiled model. In Chiwawa, WA the forest tile contained relatively slow melt rates due to increased shortwave radiation attenuation from relatively tall trees, and snow disappeared 24 days later compared to the non-tiled model. As a result, late-season streamflow increased by 15% using the tiled model, compared to the non-tiled model.

Representing forest-SWE variability did not notably affect annual evapotranspiration amounts. Therefore, differences in forest-snow processes between the tiled and non-tiled model were generally linked to changes in streamflow rather than changes in evapotranspiration. Within all three watersheds, similar results were found when the tiled model did not account for forest edges and only simulated forest and exposed tiles, suggesting that forest edges within the existing forest structure do not substantially affect late-season streamflow simulations. However, explicitly representing differences between snow directly underneath the canopy and exposed areas did affect streamflow in the Jemez and Chiwawa.

Representing forest edges can be critical for properly simulating late-season streamflow in certain climates when the forest edge represents a substantial fractional area. For instance, in the Chiwawa, a synthetic silvicultural practice that maximized the fractional area of north-facing forest edges resulted in an increase of August-September streamflow by 36-38% relative to a tiled model configuration that only represented forested and exposed tiles.

Therefore, when representing forest-SWE variability within the existing forest structure, there was an effect on late-season streamflow in some watersheds but not in others based on the fractional area of forest edges, forest characteristics, and the climate conditions. We encourage hydrologic modelers to carefully consider their watershed's characteristics and climate to determine whether resolving forest-SWE variability is applicable. Lastly, we encourage those interested in forest restoration efforts to use the tiled model as an additional tool to understand how forest management strategies affect streamflow.

7. Acknowledgements

We gratefully acknowledge funding support from a NASA Earth and Space Sciences Fellowship, Grant NNX16AO02H. Jessica D. Lundquist, Mark Wigmosta, Ning Sun, and Nicoleta Cristea, were supported by NSF Grant CBET-1703663. We would like to thank Tobias Jonas, Bart Nijssen, Mimi Hughes, and Cassie Lumbrazo for comments on an early version of this work.

8. Data Availability

The tiled model code within DHSVM is publicly available here: https://github.com/wcurrier/DHSVM-PNNL. Airborne Snow Observatory Data for the Tuolumne Watershed were accessed from: https://nsidc.org/data/aso/data-summaries. CDWR data were provided from: http://cdec.water.ca.gov/. SNOTEL data were accessed from: https://www.wcc.nrcs.usda.gov/snow/. A description of how to derive shortwave and longwave radiation data using MTCLIM can be found at https://github.com/UW-Hydro/MetSim. NCALM lidar data were provided from http://opentopography.org/. ASO data are available at https://nsidc.org/data/aso/data-summaries. Chiwawa lidar data can be found at: https://lidarportal.dnr.wa.gov/. Livneh data can be downloaded at https://www.esrl.noaa.gov/psd/data/gridded/data.livneh.html. WRF data for Jemez can be downloaded at: https://rda.ucar.edu/datasets/ds612.0/. CUES data can be downloaded from: https://snow.ucsb.edu/index.php/level-2-model-ready/. Tuolumne streamflow and forcing data can be downloaded from: https://depts.washington.edu/mtnhydr/Pages/Data/yosemite.shtml. All other data that were not publicly available but used within this paper were uploaded to a Zenodo repository at: (to be finalized after review of this manuscript).

9. References

Andreadis, K. M., Storck, P., & Lettenmaier, D. P. (2009). Modeling snow accumulation and ablation processes in forested environments. *Water Resources Research*, *45*(5), 1–13. https://doi.org/10.1029/2008WR007042

Biederman, J. A., Brooks, P. D., Harpold, A. A., Gochis, D. J., Gutmann, E., Reed, D. E., et al. (2014). Multiscale observations of snow accumulation and peak snowpack following widespread, insect-induced lodgepole pine mortality. *Ecohydrology*, *7*(1), 150–162. https://doi.org/10.1002/eco.1342

Brandle, J.R., Finch, S. (1991). How windbreaks work. *Natural Resourses, Nebraska Cooperative Extension Service*. National Agroforesty Center. https://doi.org/EC 91-1763-B

Brauchli, T., Trujillo, E., Huwald, H., & Lehning, M. (2017). Influence of Slope-Scale Snowmelt on Catchment Response Simulated With the *Alpine3D* model. *Water Resources Research*. https://doi.org/10.1002/2017WR021278

Broxton, P. D., Harpold, A. A., Biederman, J. A., Troch, P. A., Molotch, N. P., & Brooks, P. D. (2015). Quantifying the effects of vegetation structure on snow accumulation and ablation in mixed-conifer forests. *Ecohydrology*, *8*(6), 1073–1094. https://doi.org/10.1002/eco.1565

Churchill, D. J., Larson, A. J., Dahlgreen, M. C., Franklin, J. F., Hessburg, P. F., & Lutz, J. A. (2013). Restoring forest resilience: From reference spatial patterns to silvicultural prescriptions and monitoring. *Forest Ecology and Management*, *291*, 442–457. https://doi.org/10.1016/j.foreco.2012.11.007

Clark, M. P., Hendrikx, J., Slater, A. G., Kavetski, D., Anderson, B., Cullen, N. J., et al. (2011). Representing spatial variability of snow water equivalent in hydrologic and land-surface models: A review. *Water Resources Research*, *47*(7).

https://doi.org/10.1029/2011WR010745

Cristea, N. C., Lundquist, J. D., Loheide, S. P., Lowry, C. S., & Moore, C. E. (2014). Modelling how vegetation cover affects climate change impacts on streamflow timing and magnitude in the snowmelt-dominated upper Tuolumne Basin, Sierra Nevada. *Hydrological Processes*, *28*(12), 3896–3918. https://doi.org/10.1002/hyp.9909

Cuo, L., Giambelluca, T. W., & Ziegler, A. D. (2011). Lumped parameter sensitivity analysis of a distributed hydrological model within tropical and temperate catchments. *Hydrological Processes*, *25*(15), 2405–2421. https://doi.org/10.1002/hyp.8017

Currier, W. R., & Lundquist, J. D. (2018). Snow Depth Variability at the Forest Edge in Multiple Climates in the Western United States. *Water Resources Research*, *54*, 1–18. https://doi.org/10.1029/2018WR022553

Currier, W. R., Pflug, J., Mazzotti, G., Jonas, T., Deems, J. S., Bormann, K. J., et al. (2019). Comparing aerial lidar observations with terrestrial lidar and snow-probe transects from NASA's 2017 SnowEx campaign. *Water Resources Research*, 1–10. https://doi.org/10.1029/2018wr024533

Daly, C., Halbleib, M., Smith, J. I., Gibson, W. P., Doggett, M. K., Taylor, G. H., et al. (2008). Physiographically sensitive mapping of climatological temperature and precipitation across the conterminous United States. *International Journal of Climatology*, *28*(15), 2031–2064. https://doi.org/10.1002/joc.1688

Department of Natural Resources, W. S. (2020). Washington Lidar Portal. Washington State Department of Natural Resources. Retrieved from https://lidarportal.dnr.wa.gov/

Dickerson-Lange, S. E., Lutz, J. A., Gersonde, R., Martin, K. A., Forsyth, J. E., & Lundquist, J. D. (2015). Observations of distributed snow depth and snow duration within diverse forest

structures in a maritime mountain watershed. *Water Resources Research*, *51*(11), 9353–9366. https://doi.org/10.1002/2015WR017873

Dickerson-Lange, S. E., Gersonde, R. F., Hubbart, J. A., Link, T. E., Nolin, A. W., Perry, G. H., et al. (2017). Snow disappearance timing is dominated by forest effects on snow accumulation in warm winter climates of the Pacific Northwest, United States. *Hydrological Processes*, *31*(10), 1846–1862. https://doi.org/10.1002/hyp.11144

Dickerson-Lange, S. E., Vano, J. A., Gersonde, R., & Lundquist, J. D. (2021). Ranking Forest Effects on Snow Storage: A Decision Tool for Forest Management. *Water Resources Research*, *57*(10). https://doi.org/10.1029/2020WR027926

Dingman, L. (2002). *Physical Hydrology* (2nd ed.). Long Grove, Illinois: Waveland Press, Inc.

Du, E., Link, T. E., Gravelle, J. A., & Hubbart, J. A. (2014). Validation and sensitivity test of the distributed hydrology soil-vegetation model (DHSVM) in a forested mountain watershed. *Hydrological Processes*, *28*(26), 6196–6210. https://doi.org/10.1002/hyp.10110

Golding, D. L., & Swanson, R. H. (1978). Snow accumulation and melt in small forest openings in Alberta. *Canadian Journal of Forest Research*, *8*(4), 380–388. https://doi.org/10.1139/x78-057

Harpold, A A, Guo, Q., Molotch, N., Brooks, P. D., Bales, R., Fernandez-Diaz, J. C., et al. (2014). LiDAR-derived snowpack data sets from mixed conifer forests accross the Western United States. *Water Resources Research*, *50*(October 2013), 2749–2755. https://doi.org/10.1002/2013WR013935.Received

Harpold, Adrian A., Biederman, J. A., Condon, K., Merino, M., Korgaonkar, Y., Nan, T., et al. (2014). Changes in snow accumulation and ablation following the Las Conchas Forest Fire, New Mexico, USA. *Ecohydrology*, *7*(2), 440–452. https://doi.org/10.1002/eco.1363

Harpold, Adrian A., Molotch, N. P., Musselman, K. N., Bales, R. C., Kirchner, P. B., Litvak, M., & Brooks, P. D. (2015). Soil moisture response to snowmelt timing in mixed-conifer subalpine forests. *Hydrological Processes*, *29*(12), 2782–2798. https://doi.org/10.1002/hyp.10400

Haugo, R., Zanger, C., DeMeo, T., Ringo, C., Shlisky, A., Blankenship, K., et al. (2015). A new approach to evaluate forest structure restoration needs across Oregon and Washington, USA. *Forest Ecology and Management*, *335*, 37–50. https://doi.org/10.1016/j.foreco.2014.09.014

Hessburg, P. F., Churchill, D. J., Larson, A. J., Haugo, R. D., Miller, C., Spies, T. A., et al. (2015). Restoring fire-prone Inland Pacific landscapes: seven core principles. *Landscape Ecology*, *30*(10), 1805–1835. https://doi.org/10.1007/s10980-015-0218-0

Hiemstra, C. A., Liston, G. E., & Reiners, W. A. (2002). Snow Redistribution by Wind and Interactions with Vegetation at Upper Treeline in the Medicine Bow Mountains, Wyoming, U.S.A. *Arctic, Antarctic, and Alpine Research*, *34*(3), 262–273.

Hiemstra, C. A., Liston, G. E., & Reiners, W. A. (2006). Observing, modelling, and validating snow redistribution by wind in a Wyoming upper treeline landscape. *Ecological Modelling*, *197*(1–2), 35–51. https://doi.org/10.1016/j.ecolmodel.2006.03.005

Homer, C. G., Dewitz, J. A., Yang, L., Jin, S., Danielson, P., Xian, G., et al. (2015). Completion of the 2011 National Land Cover Database for the conterminous United States-Representing a decade of land cover change information. *Photogrammetric Engineering and Remote Sensing*, *81*(5), 345–354.

Huemmrich, K. F., & Goward, S. N. (1997). Vegetation canopy PAR absorptance and NDVI: An assessment for ten tree species with the SAIL model. *Remote Sensing of Environment*,

61(2), 254–269. https://doi.org/10.1016/S0034-4257(97)00042-4

Lawler, R. R., & Link, T. E. (2011). Quantification of incoming all-wave radiation in discontinuous forest canopies with application to snowmelt prediction. *Hydrological Processes*, *25*(21), 3322–3331. https://doi.org/10.1002/hyp.8150

Luce, C. H., Tarboton, D. G., & Cooley, K. R. (1998). The infuence of the spatial distribution of snow on basin-averaged snowmelt\r. *Hydrological Processes*, *12*(May 1997), 1671–1683. https://doi.org/10.1002/(SICI)1099-1085(199808/09)12:10/11<1671::AID-HYP688>3.0.CO;2-N

Lundquist, J. D., & Dettinger, M. D. (2005). How snowpack heterogeneity affects diurnal streamflow timing. *Water Resources Research*, *41*(5), 1–14. https://doi.org/10.1029/2004WR003649

Lundquist, J. D., Dettinger, M. D., & Cayan, D. R. (2005). Snow-fed streamflow timing at different basin scales: Case study of the Tuolumne River above Hetch Hetchy, Yosemite, California. *Water Resources Research*, *41*(7), 1–14. https://doi.org/10.1029/2004WR003933

Lundquist, J. D., Dickerson-Lange, S. E., Lutz, J. A., & Cristea, N. C. (2013). Lower forest density enhances snow retention in regions with warmer winters: A global framework developed from plot-scale observations and modeling. *Water Resources Research*, *49*(10), 6356–6370. https://doi.org/10.1002/wrcr.20504

Lundquist, J. D., Roche, J. W., Forrester, H., Moore, C., Keenan, E., Perry, G., et al. (2016). Yosemite Hydroclimate Network: Distributed stream and atmospheric data for the Tuolumne River watershed and surroundings. *Water Resources Research*, *52*(9), 7478–7489. https://doi.org/10.1002/2016WR019261

Mazzotti, G., Currier, W. R., Deems, J. S., Pflug, J. M., Lundquist, J. D., & Jonas, T. (2019). Revisiting Snow Cover Variability and Canopy Structure Within Forest Stands: Insights From Airborne Lidar Data. *Water Resources Research*, *55*(7), 6198–6216. https://doi.org/10.1029/2019wr024898

Mazzotti, G., Essery, R., Moeser, C. D., & Jonas, T. (2020). Resolving Small-Scale Forest Snow Patterns Using an Energy Balance Snow Model With a One-Layer Canopy. *Water Resources Research*, *56*(1). https://doi.org/10.1029/2019WR026129

Mazzotti, G., Webster, C., Essery, R., & Jonas, T. (2021). Increasing the Physical Representation of Forest-Snow Processes in Coarse-Resolution Models: Lessons Learned From Upscaling Hyper-Resolution Simulations. *Water Resources Research*, *57*(5). https://doi.org/10.1029/2020WR029064

Meyer, P. D., Rockhold, M. L., Gee, G. W., & Nicholson, T. J. (1997). Uncertainty Analyses of Infiltration and Subsurface Flow and Transport for SDMP Sites Uncertainty Analyses of Infiltration and Subsurface Flow and Transport for SDMP Sites. *Nureg/Cr*, *NUREG/CR-6*, 85.

Moeser, D., Mazzotti, G., Helbig, N., & Jonas, T. (2016). Representing spatial variability of forest snow: Implementation of a new interception model. *Water Resources Research*, *52*(2), 1208–1226. https://doi.org/10.1002/2015WR017961

Molotch, N. P., Brooks, P. D., Burns, S. P., Litvak, M., Monson, R. K., McConnell, J. R., & Musselman, K. N. (2009). Ecohydrological controls on snowmelt partitioning in mixed-conifer sub-alpine forests. *Ecohydrology*, *2*(2), 129–142. https://doi.org/10.1002/eco.48

Monteith, J. L. (1965). Rothamsted Repository Download. *Symposia of the Society for Experimental Biology*, (19), 205–234.

Musselman, K. N., & Pomeroy, J. W. (2017). Estimation of Needleleaf Canopy and Trunk Temperatures and Longwave Contribution to Melting Snow. *Journal of Hydrometeorology*, *18*(2), 555–572. https://doi.org/10.1175/JHM-D-16-0111.1

Musselman, K. N., Molotch, N. P., & Brooks, P. D. (2008). Effects of vegetation on snow accumulation and ablation in a mid-latitude sub-alpine forest. *Hydrological Processes*, *22*(15), 2767–2776. https://doi.org/10.1002/hyp.7050

Musselman, K. N., Pomeroy, J. W., & Link, T. E. (2015). Variability in shortwave irradiance caused by forest gaps: Measurements, modelling, and implications for snow energetics. *Agricultural and Forest Meteorology*, *207*, 69–82. https://doi.org/10.1016/j.agrformet.2015.03.014

Painter, T. H., Berisford, D. F., Boardman, J. W., Bormann, K. J., Deems, J. S., Gehrke, F., et al. (2016). The Airborne Snow Observatory: Fusion of scanning lidar, imaging spectrometer, and physically-based modeling for mapping snow water equivalent and snow albedo. *Remote Sensing of Environment*, *184*(July), 139–152. https://doi.org/10.1016/j.rse.2016.06.018

Sexstone, G. A., Driscoll, J. M., Hay, L. E., Hammond, J. C., & Barnhart, T. B. (2020). Runoff sensitivity to snow depletion curve representation within a continental scale hydrologic model. *Hydrological Processes*, hyp.13735. https://doi.org/10.1002/hyp.13735

Seyednasrollah, B., & Kumar, M. (2014). Journal of Geophysical Research : Atmospheres, 1–20. https://doi.org/10.1002/2014JD021809.Received

Seyfried, M. S., & Wilcox, B. P. (1995). Scale and the Nature of Spatial Variability: Field Examples Having Implications for Hydrologic Modeling. *Water Resources Research*, *31*(1), 173–184. https://doi.org/10.1029/94WR02025

Small, E. E., & McConnell, J. R. (2008). Comparison of soil moisture and meteorological controls on pine and spruce transpiration. *Ecohydrology*, *1*(3), 205–214. https://doi.org/10.1002/eco.25

Storck, P. (2000). *Trees, snow and flooding: an investigation of forest canopy effects on snow accumulation and melt at the plot and watershed scales in the Pacific Northwest*. Seattle. Retrieved from https://www.ce.washington.edu/sites/cee/files/pdfs/research/hydrology/water-resources/WRS161.pdf

Storck, Pascal, Lettenmaier, D. P., & Bolton, S. M. (2002). Measurement of snow interception and canopy effects on snow accumulation and melt in a mountainous maritime climate, Oregon, United States. *Water Resources Research*, *38*(11), 5-1-5–16. https://doi.org/10.1029/2002WR001281

Sturm, M., Holmgren, J., & Liston, G. E. (1995). A seasonal snow cover classification system for local to global applications. *Journal of Climate*. https://doi.org/10.1175/1520-0442(1995)008<1261:ASSCCS>2.0.CO;2

Sturm, Matthew, Taras, B., Liston, G. E., Derksen, C., Jonas, T., & Lea, J. (2010). Estimating Snow Water Equivalent Using Snow Depth Data and Climate Classes. *Journal of Hydrometeorology*, *11*, 1380–1394. https://doi.org/10.1175/2010JHM1202.1

Sun, N., Wigmosta, M., Zhou, T., Lundquist, J., Dickerson-Lange, S., & Cristea, N. (2018). Evaluating the functionality and streamflow impacts of explicitly modeling forest-snow interactions and canopy gaps in a distributed hydrologic model. *Hydrological Processes*, 1–39. https://doi.org/10.1002/hyp.13150

Thyer, M., Beckers, J., Spittlehouse, D., Alila, Y., & Winkler, R. (2004). Diagnosing a

distributed hydrologic model for two high-elevation forested catchments based on detailed stand- and basin-scale data. *Water Resources Research*, *40*(1). https://doi.org/10.1029/2003WR002414

Varhola, A., Coops, N. C., Weiler, M., & Moore, R. D. (2010). Forest canopy effects on snow accumulation and ablation: An integrative review of empirical results. *Journal of Hydrology*, *392*(3–4), 219–233. https://doi.org/10.1016/j.jhydrol.2010.08.009

WDNR. (2018). *20-Year Forest Health Strategic Plan: Eastern Washington*. Olympia, WA. Retrieved from https://www.dnr.wa.gov/ForestHealthPlan

Webb, R. W., Raleigh, M. S., McGrath, D., Molotch, N. P., Elder, K., Hiemstra, C., et al. (2020). Within-Stand Boundary Effects on Snow Water Equivalent Distribution in Forested Areas. *Water Resources Research*, *56*(10). https://doi.org/10.1029/2019WR024905

Webster, C., Rutter, N., Zahner, F., & Jonas, T. (2016). Measurement of Incoming Radiation below Forest Canopies: A Comparison of Different Radiometer Configurations. *Journal of Hydrometeorology*, *17*(3), 853–864. https://doi.org/10.1175/JHM-D-15-0125.1

Webster, C., Rutter, N., & Jonas, T. (2017). Improving representation of canopy temperatures for modeling subcanopy incoming longwave radiation to the snow surface. *Journal of Geophysical Research: Atmospheres*, *122*(17), 9154–9172. https://doi.org/10.1002/2017JD026581

Wigmosta, M., Duan, Z., Coleman, A., & Skaggs, R. (2015). *Development of a distributed hydrology model for use in a forest restoration decision support tool to increase snowpack in the upper Columbia*. Richland, WA. Retrieved from https://www.ucsrb.org/?mdocs-file=7920

Wigmosta, M. S., Vail, L. W., & Lettenmaier, D. P. (1994). A distributed hydrology-vegetation

model for complex terrain. *Water Resources Research*, *30*(6), 1665–1679. https://doi.org/10.1029/94WR00436

Wigmosta, M. S., Nijssen, B., & Storck, P. (2002). The distributed hydrology soil vegetation model. *Mathematical Models of Small Watershed Hydrology and Applications*, 7–42. Retrieved from http://www.cabdirect.org/abstracts/20033121322.html

Woo, M. K., & Giesbrecht, M. A. (2000). Simulation of snowmelt in a subarctic spruce woodland: 1. Tree model. *Water Resources Research*, *36*(8), 2275–2285. https://doi.org/10.1029/2000WR900094

Xiao, Q., & McPherson, E. G. (2005). Tree health mapping with multispectral remote sensing data at UC Davis, California. *Urban Ecosystems*, *8*(3–4), 349–361. https://doi.org/10.1007/s11252-005-4867-7

Zhao, Q., Liu, Z., Ye, B., Qin, Y., Wei, Z., & Fang, S. (2009). A snowmelt runoff forecasting model coupling WRF and DHSVM. *Hydrology and Earth System Sciences*, *13*(10), 1897–1906. https://doi.org/10.5194/hess-13-1897-2009

Tables

Table 1: Meteorological and watershed forest characteristics. †Mean tree height was calculated where lidar data was available within the watershed and the average height where vegetation was greater than 2 m. ‡Fraction of the watershed that is forested based on high-resolution (1-3 m) maps from NAIP imagery and lidar. §Fraction of the watershed that is forested based on a coarsened (90-150 m) NLCD vegetation map.

	Upper Tuolumne River Watershed, CA	**Jemez River Watershed, NM**	**Chiwawa River Watershed, WA**
General Watershed and Meteorological Statistics			
Watershed Size [km^2]	186	1222	446
Median and Range in Elevation [m]	3158 1314	2612 1719	1365 2034
Average Incoming Shortwave Radiation (Nov-April) [W m^{-2}]	175	223	153
Mean Winter Temperature (Nov-Mar) [°C]	-5.2	-3.0	-5.5
Basin Total Winter Precipitation (Nov-Mar) [mm]	723	324	1154
Vegetation Characteristics I: Calculations based on high-resolution (1-3 m) vegetation maps derived from lidar or NAIP imagery.			
Mean Tree Height [m] †	8.3	10.2	17
Watershed Fraction‡ : Forested	33%	46%	80%
Watershed Fraction: North-Facing Edge	4%	17%	2%
Watershed Fraction: South-Facing Edge	1%	1%	2%
Watershed Fraction: Exposed	62%	36%	16%
Vegetation Characteristics II: Calculations based on coarsened (90-150 m) grid cells.			
Fraction of Watershed§: Forested	45%	80%	84%
Average fraction of forest grid cells: Forested (Forest Density)	69%	59%	87%
Average fraction of forest grid cells: North Facing	6%	20%	2%
Average fraction of forest grid cells: South Facing	2%	1%	2%
Average fraction of forest grid cells: Exposed	23%	19%	11%

Table 2: Parameters introduced to model forest edges at Tuolumne, CA and Jemez, NM. See Section 3.c. for more details.

Parameters introduced to model the forest edges	**Tuolumne, CA**	**Jemez, NM**
Fractional North Facing Coverage (F_{sf}) *Controls the amount longwave radiation received at the north facing edge*	**0.15**	**0.4**
Fractional South Facing Coverage (F_{nf}) *Controls the amount longwave radiation received at the south facing edge*	**0.2**	**0.4**
Diffuse Radiation Attenuation NF (τ_{nf}) *Extinction of diffuse radiation at the north facing edge*	**0.75**	**0.75**
Diffuse Radiation Attenuation SF (τ_{sf}) *Extinction of diffuse radiation at the south facing edge*	**0.75**	**0.75**
NF Edge Radiation Multiplier (τ_{mult}) *Used to provide more direct beam radiation on the north-facing edge than directly underneath the forest*	**1.0**	**0.2**

Table 3: Simulated peak SWE, snow disappearance date (SDD), and melt rates (Peak SWE divided by number of days between peak SWE and SDD) for each tile component and the non-tiled model at the evaluation grid cell in each watershed. †Average from the Jemez and Tuolumne Parameters

Tuolumne, CA: Dana Meadows South	**Peak SWE** [mm]	**SDD** [YYYY-MM-DD]	**Melt Rate** [mm/day]
Non-Tiled Model	539	2016-06-07	8.1
Tiled Model Average	531	2016-06-08	6.8
North Facing	638	2016-06-07	9.6
South Facing	500	2016-05-19	7.9
Forest	455	2016-06-08	5.8
Exposed	595	2016-06-04	8.0
Jemez, NM: Evaluation Site	--	--	--
Non-Tiled Model	291	2010-05-16	5.8
Tiled Model Average	281	2010-05-16	5.6
North Facing	334	2010-05-16	6.6
South Facing	267	2010-04-16	8.4
Forest	213	2010-05-12	4.6
Exposed	328	2010-05-08	7.8
Chiwawa, WA: Evaluation Site†	--	--	--
Non-Tiled Model	860	2011-05-31	13.6
Tiled Model Average	842	2011-07-07	8.5
North Facing	1320	2011-07-07	18.3
South Facing	1002	2011-05-11	19.3
Forest	747	2011-06-23	12.8
Exposed	1067	2011-05-15	8.2

Figure Legends

Figure 1: A) Deeper snow north of the canopy mask, with shallower snow on the south-side of the trees in Jemez Caldera, NM, USA. B) Spatial heterogeneity of snow is accounted for with four simulated snowpacks per grid cell driven by unique radiation conditions. Each snowpack accumulates and melts independently, providing water to a shared 3-layer soil reservoir.

Figure 2: Basin delineations, fractional forest maps derived from lidar, NAIP, and NLCD 2011 data used within the non-tiled and tiled version of DHSVM for three different watersheds. Watersheds organized based on elevation. Snow pillow locations were used for evaluating SWE simulations in exposed areas during model calibration in addition to the streamflow locations. The tiled model was evaluated at the evaluation sites.

Figure 3: Example of using NAIP imagery to calculate NDVI and subsequently create a canopy mask. The resulting classification map used methods described in (Currier & Lundquist, 2018) to classify north (NF) and south-facing (SF) edges, in addition to exposed (EXP) and forest (FOR) areas. NAIP imagery agreed at 80 percent of the pixels within the 2-km domain. The classification map was further masked out using NLCD 2011 vegetation classifications (Section 2.d.). Classification map shown in Figure 3 is before masking with the NLCD 2011 map. Black lines on the classification map represent 150-m grid boxes.

Figure 4: Example of direct beam radiation for different components of the tiled model. Equations 7-10 were based on the equation for net shortwave radiation at the understory in the non-tiled DHSVM shown here (Equation 1).

Figure 5: Model tuning results at snow pillow and stream gages (Figure 1). Top Row: Upper Tuolumne simulations during an average water year – WY 2016. Middle Row: Jemez River Watershed in WY 2010 when lidar observations of snow depth exist. Bottom Row: Chiwawa, WA watershed simulations of SWE and streamflow.

Figure 6: a-b) Simulated SWE within a single grid cell for individual tiles compared to lidar-derived SWE estimates (mean of all classified lidar pixels within the DHSVM grid cell) as well as grid cell average SWE (amongst the four tiles) and the non-tiled model's simulation of SWE with the same forest configuration for Tuolumne, CA and Jemez, NM. c-j) Different components of the energy balance for individual tile components. Note: The tiled model's average radiation (weighted by the fractional area of each tile) was not used within the tiled model but is shown for comparison.

Figure 7: a-b) Simulated cumulative hydrologic fluxes between the tiled model (dotted lines) and the non-tiled model (solid lines) for an individual grid cell within the Tuolumne, CA and Jemez, NM watersheds. Hydrologic fluxes were overlaid with the SWE simulations shown in Figure 6, to show the timing of individual fluxes. Legend for simulated and observed SWE in plots a and b shown in the Jemez, NM plot. Note: Difference in scale along the y-dimension between a and b. c-d) Fractional soil moisture between the tiled model and the non-tiled model. e-f) Cumulative sublimation rates from the snowpack for individual components of the tiled model and the non-tiled model.

Figure 8: Top row: Basin average SWE for individual tile components along with basin average evapotranspiration. Note: Basin average SWE for the non-tiled model, d model average, and exposed area represent SWE in grid cells that are not tiled as well as they include non-forested areas. For instance, the tiled model was only run where the grid cells were forested. Middle row: Simulated daily streamflow values between the non-tiled and tiled model compare to observed streamflow. Bottom row: The streamflow ratio between the tiled model and non-tiled model.

Figure 9: a-b) Simulated SWE for individual tile components at the evaluation site (Figure 1). Top left uses model parameters introduced for the tiled model from Tuolumne, CA while the top right uses parameters from Jemez, NM (Table 3). c) Simulated daily streamflow values between the non-tiled and tiled model (with both the Tuolumne and Jemez parameters) compare to observed streamflow. d) The streamflow ratio between the tiled model and non-tiled model for both configuration of the tiled model in Chiwawa, WA.

Figure 10: a) Conceptual diagram of the forest management strategy within an individual tiled model grid cell. Note: the grid cell is not drawn to scale, exaggerated length wise. b) Simulated daily streamflow values with different model configurations compared to observed streamflow. Note: Tiled model with Tuolumne parameters is not shown due to similarity in results to the tile model with Jemez parameters. c) Streamflow ratio between tiled model with a managed forest and the tiled model without forest edges and a managed forest.

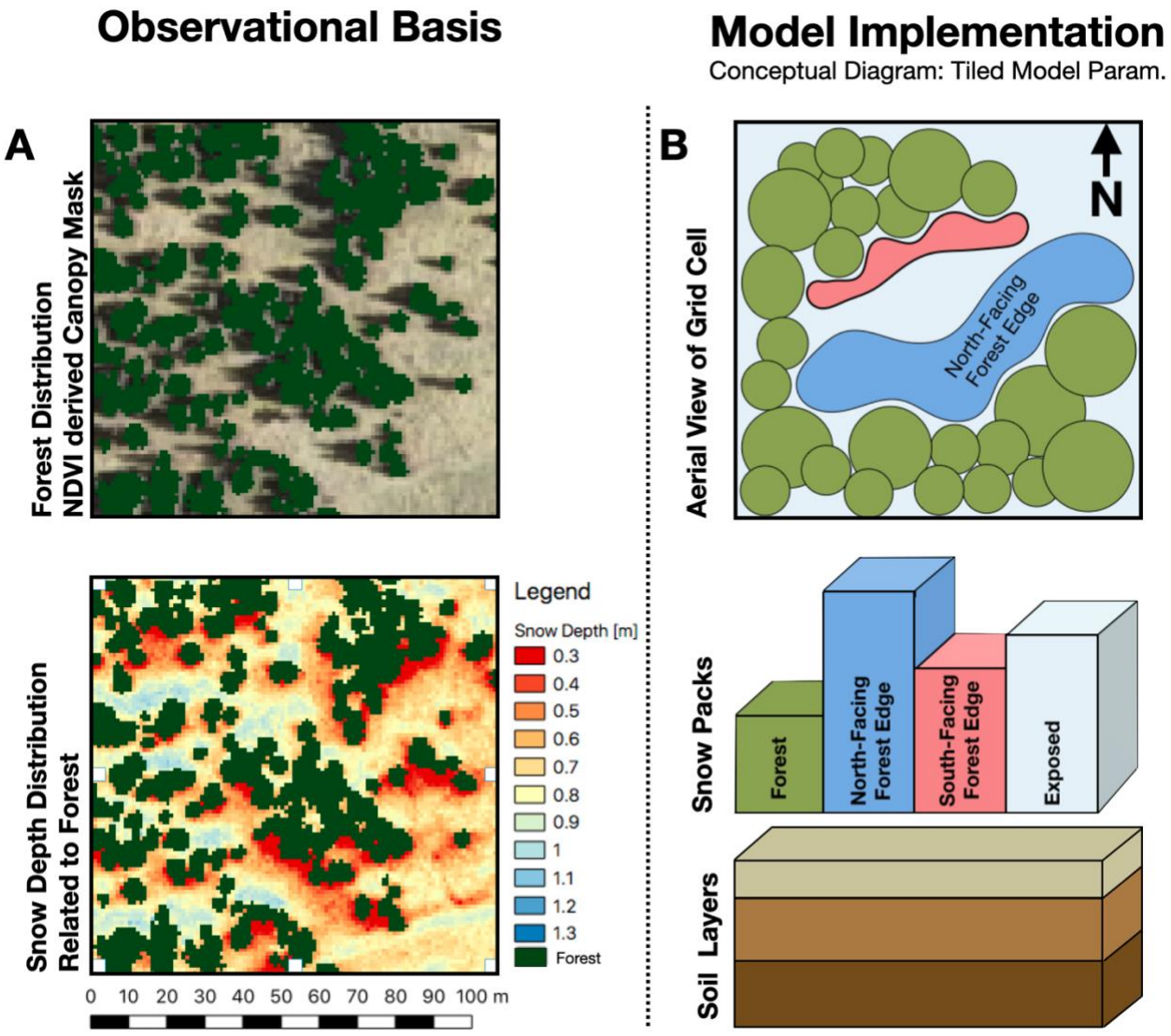

Figure 1: A) Deeper snow north of the canopy mask, with shallower snow on the south-side of the trees in Jemez Caldera, NM, USA. B) Spatial heterogeneity of snow is accounted for with four simulated snowpacks per grid cell driven by unique radiation conditions. Each snowpack accumulates and melts independently, providing water to a shared 3-layer soil reservoir.

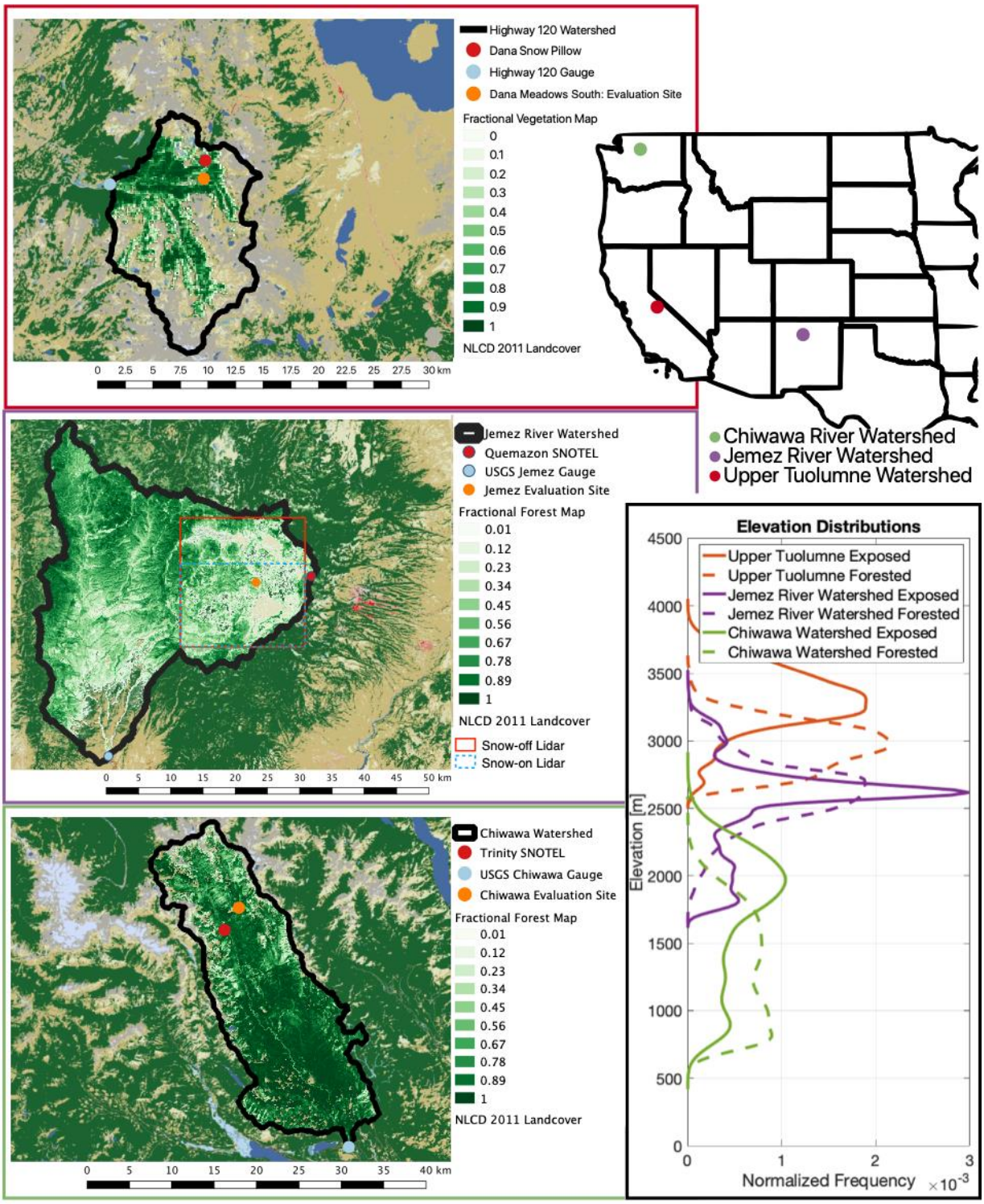

Figure 2: Basin delineations, fractional forest maps derived from lidar, NAIP, and NLCD 2011 data used within the non-tiled and tiled version of DHSVM for three different watersheds. Watersheds organized based on elevation. Snow pillow locations were used for evaluating SWE simulations in exposed areas during model calibration in addition to the streamflow locations. The tiled model was evaluated at the evaluation sites.

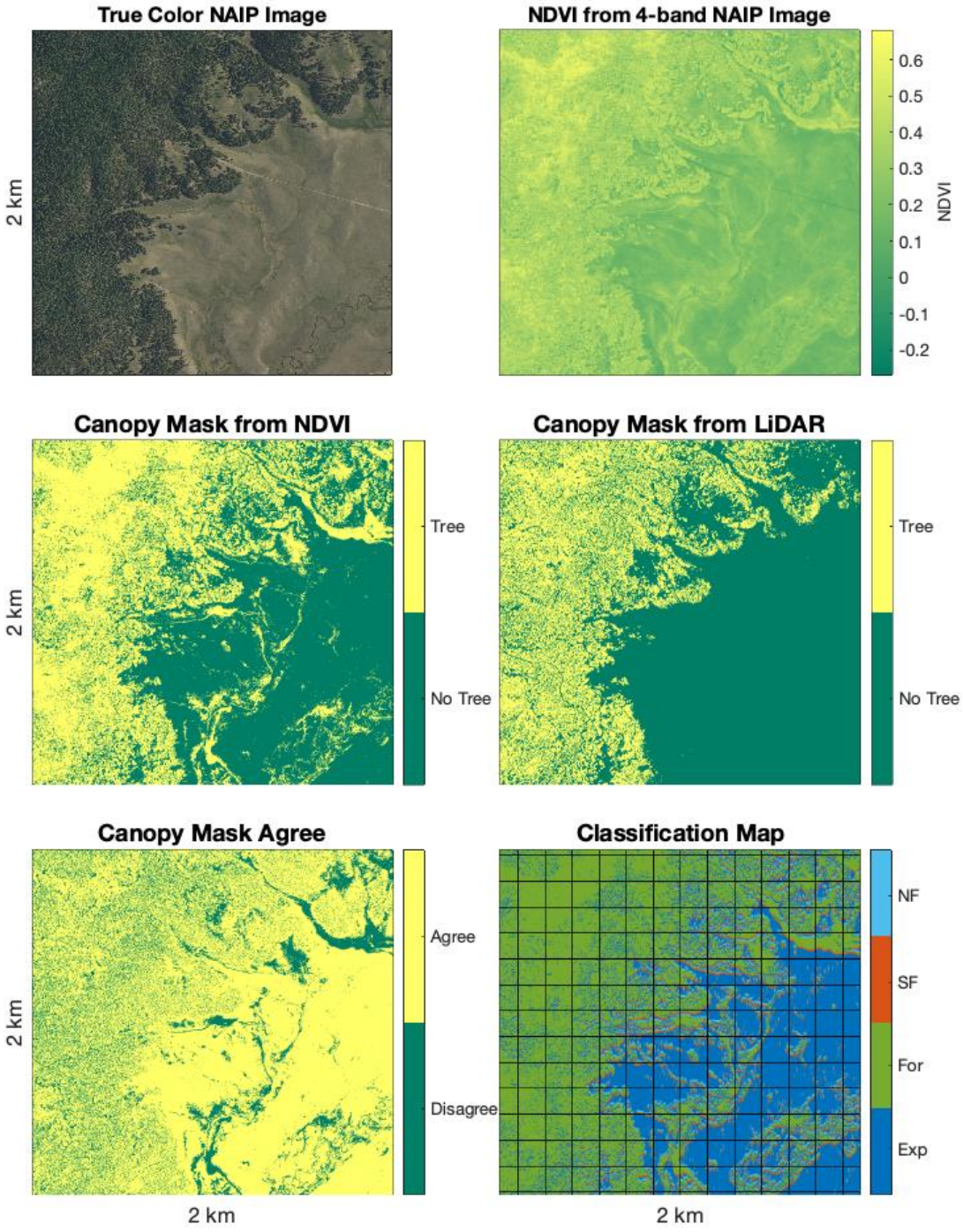

Figure 3: Example of using NAIP imagery to calculate NDVI and subsequently create a canopy mask. The resulting classification map used methods described in (Currier & Lundquist, 2018) to classify north (NF) and south-facing (SF) edges, in addition to exposed (EXP) and forest (FOR) areas. NAIP imagery agreed at 80 percent of the pixels within the 2-km domain. The classification map was further masked out using NLCD 2011 vegetation classifications (Section

2.d.). Classification map shown in Figure 3 is before masking with the NLCD 2011 map. Black lines on the classification map represent 150-m grid boxes.

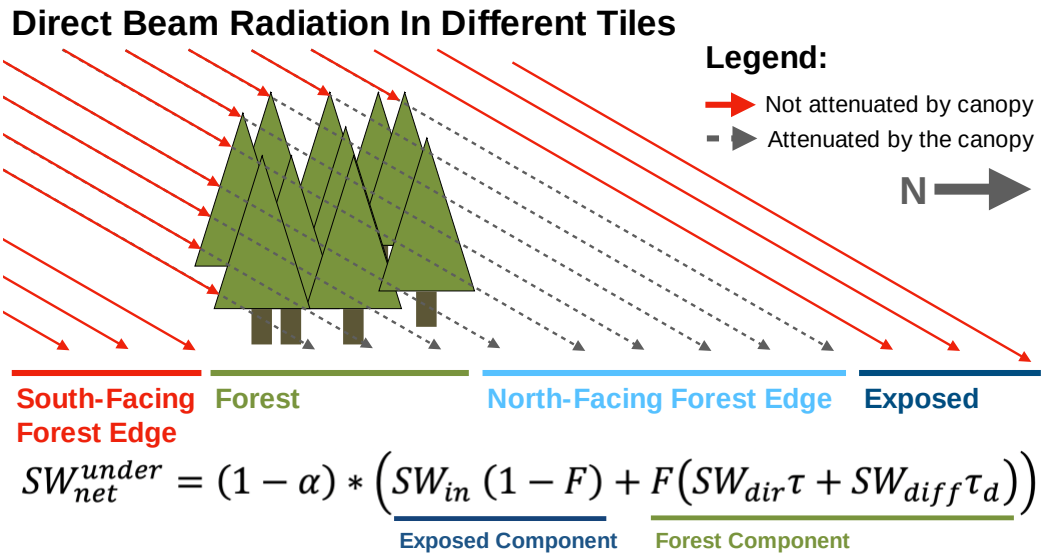

Figure 4: Example of direct beam radiation for different components of the tiled model. Equations 7-10 were based on the equation for net shortwave radiation at the understory in the non-tiled DHSVM shown here (equation 1).

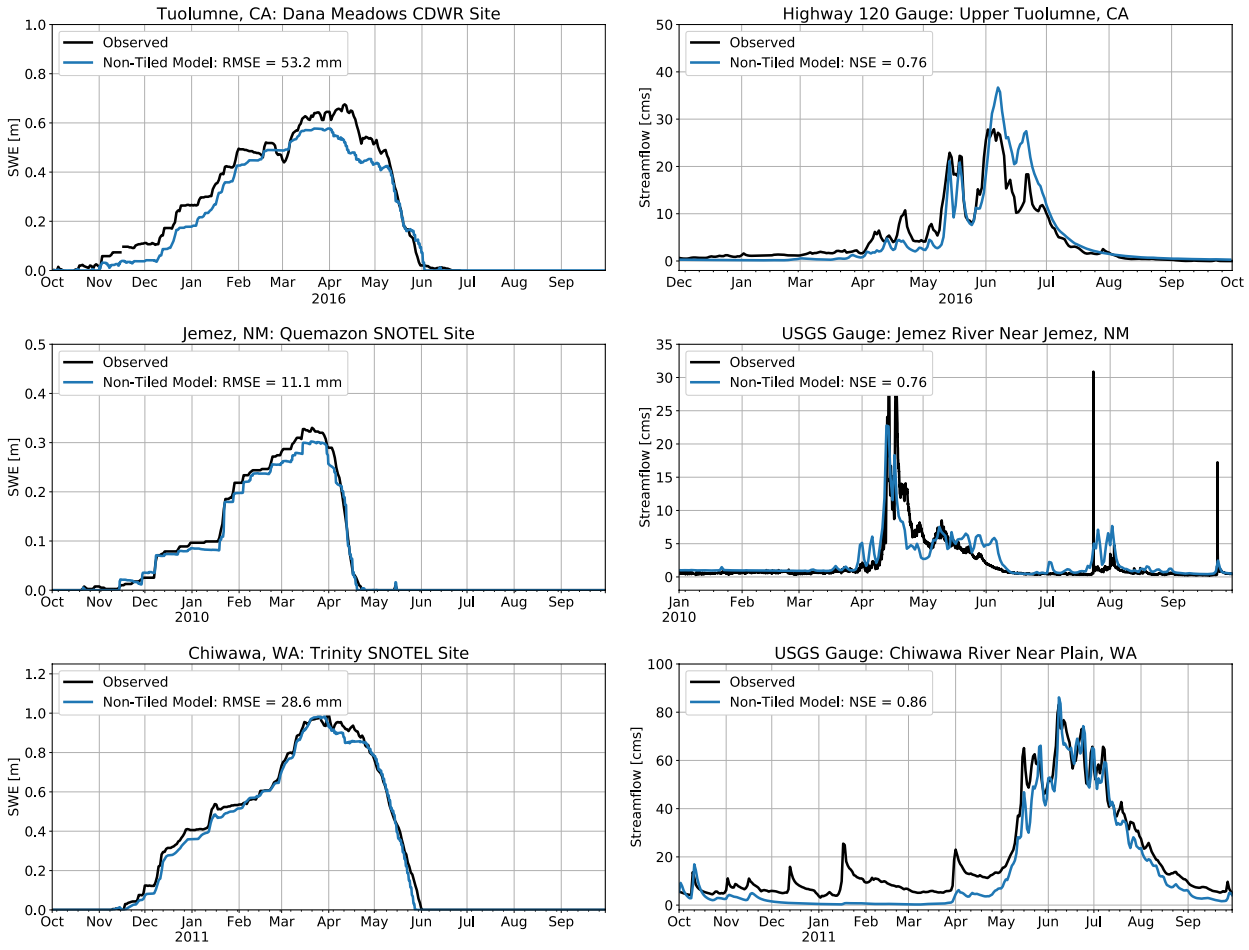

Figure 5: Model tuning results at snow pillow and stream gauges (Figure 1). Top Row: Upper Tuolumne simulations during an average water year – WY 2016. Middle Row: Jemez River Watershed in WY 2010 when lidar observations of snow depth exist. Bottom Row: Chiwawa, WA watershed simulations of SWE and streamflow.

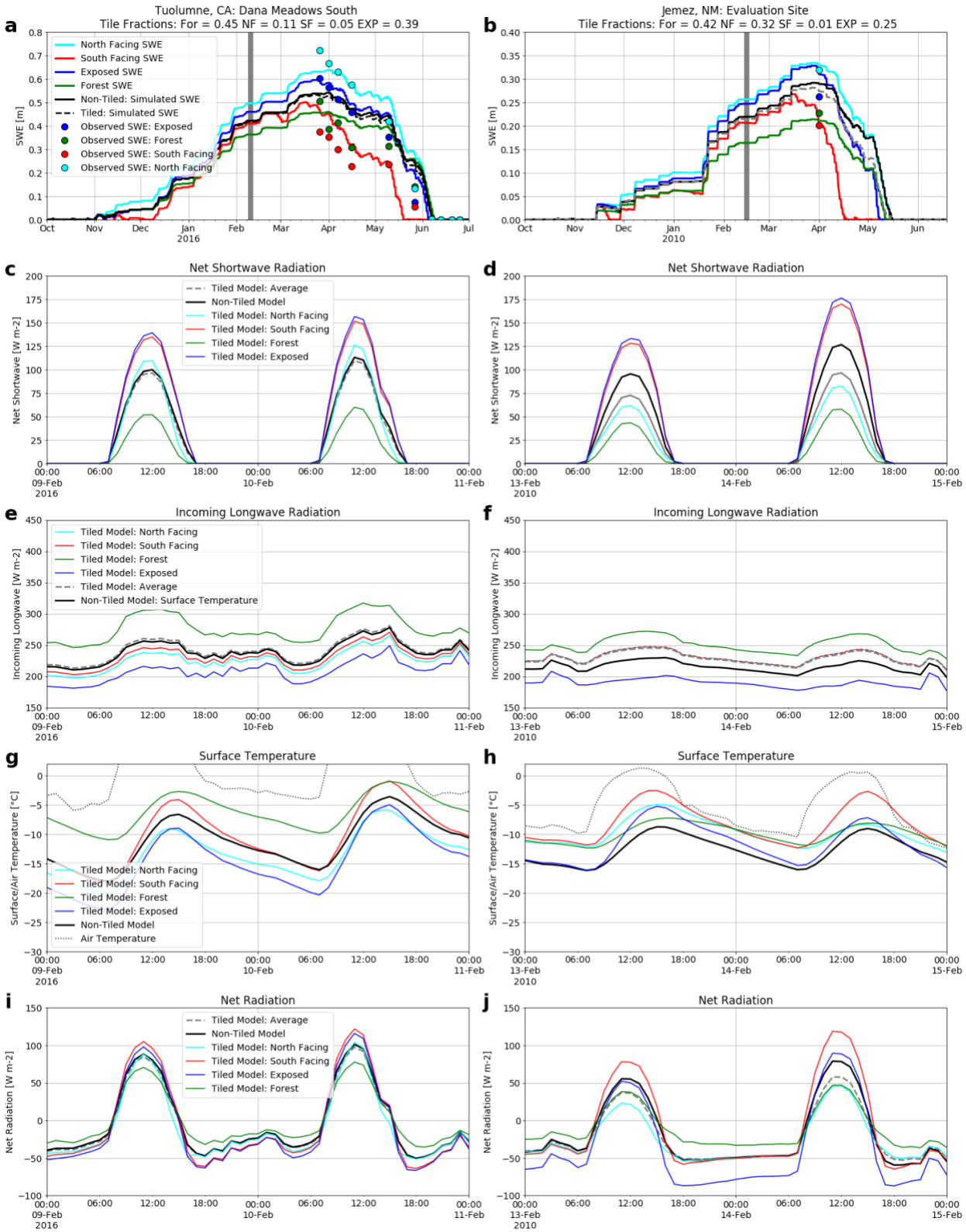
a
Tuolumne, CA: Dana Meadows South
Tile Fractions: For = 0.45 NF = 0.11 SF = 0.05 EXP = 0.39
North Facing SWE
South Facing SWE
Exposed SWE
Forest SWE
Non-Tiled: Simulated SWE
Tiled: Simulated SWE
Observed SWE: Exposed
Observed SWE: Forest
Observed SWE: South Facing
Observed SWE: North Facing
SWE [m]
b
Jemez, NM: Evaluation Site
Tile Fractions: For = 0.42 NF = 0.32 SF = 0.01 EXP = 0.25
c
Net Shortwave Radiation
Tiled Model: Average
Non-Tiled Model
Tiled Model: North Facing
Tiled Model: South Facing
Tiled Model: Forest
Tiled Model: Exposed
Net Shortwave [W m-2]
d
e
Incoming Longwave Radiation
Non-Tiled Model: Surface Temperature
Incoming Longwave [W m-2]
f
g
Surface Temperature
Surface/Air Temperature [°C]
Air Temperature
h
i
Net Radiation
Net Radiation [W m-2]
j
Oct
Nov
Dec
Jan
Feb
Mar
Apr
May
Jun
Jul
2016
2010
09-Feb
10-Feb
11-Feb
13-Feb
14-Feb
15-Feb
00:00
06:00
12:00
18:00

Figure 6: a-b) Simulated SWE within a single grid cell for individual tiles compared to lidar-derived SWE estimates (mean of all classified lidar pixels within the DHSVM grid cell) as well as grid cell average SWE (amongst the four tiles) and the non-tiled model's simulation of SWE with the same forest configuration for Tuolumne, CA and Jemez, NM. c-j) Different components of the energy balance for individual tile components. Note: The tiled model's average radiation (weighted by the fractional area of each tile) was not used within the tiled model but is shown for comparison.

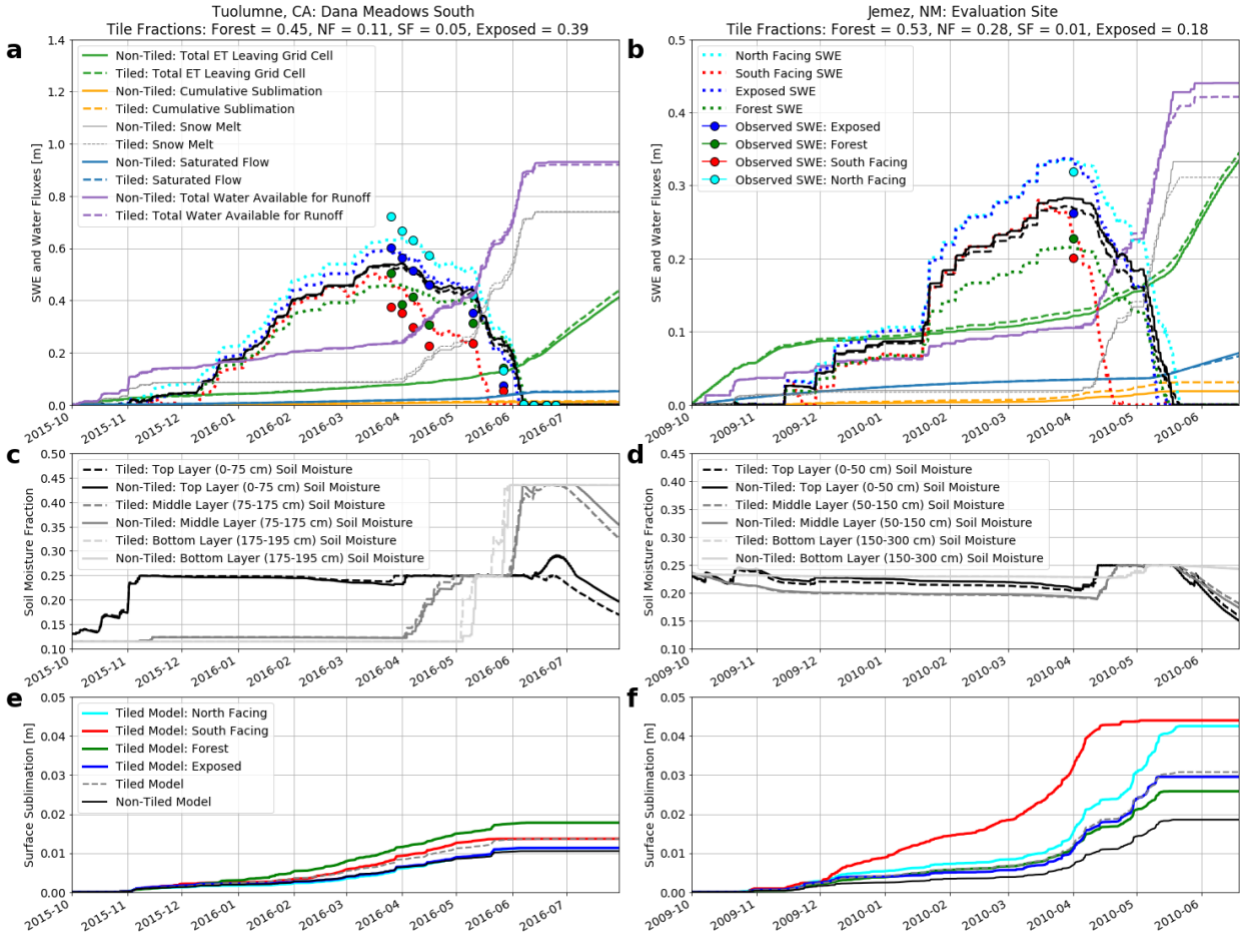

Figure 7: a-b) Simulated cumulative hydrologic fluxes between the tiled model (dotted lines) and the non-tiled model (solid lines) for an individual grid cell within the Tuolumne, CA and Jemez, NM watersheds. Hydrologic fluxes were overlaid with the SWE simulations shown in Figure 6, to show the timing of individual fluxes. Legend for simulated and observed SWE in plots a and b shown in the Jemez, NM plot. Note: Difference in scale along the y-dimension between a and b. c-d) Fractional soil moisture between the tiled model and the non-tiled model. e-f) Cumulative sublimation rates from the snowpack for individual components of the tiled model and the non-tiled model.

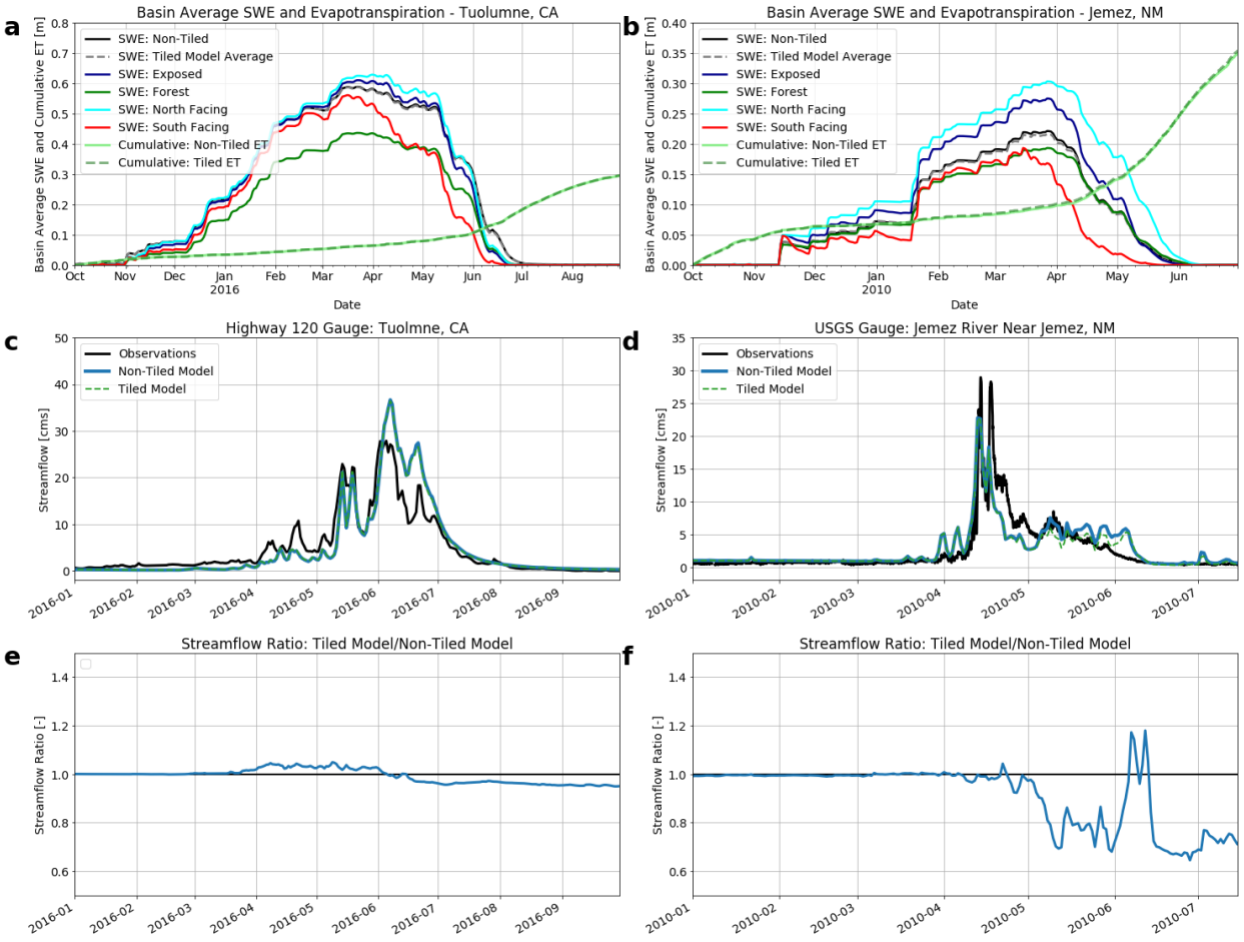

Figure 8: Top row: Basin average SWE for individual tile components along with basin average evapotranspiration. Note: Basin average SWE for the non-tiled model, d model average, and exposed area represent SWE in grid cells that are not tiled as well as they include non-forested areas. For instance, the tiled model was only run where the grid cells were forested. Middle row: Simulated daily streamflow values between the non-tiled and tiled model compare to observed streamflow. Bottom row: The streamflow ratio between the tiled model and non-tiled model.

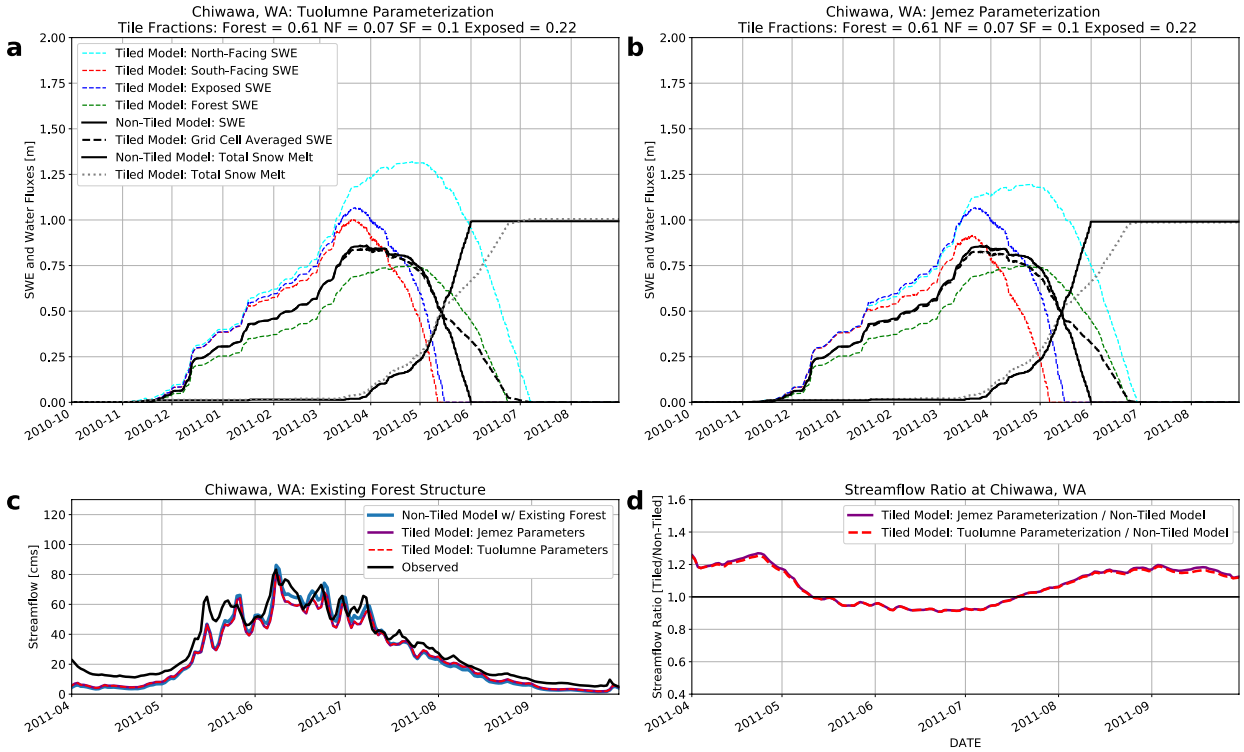

Figure 9: a-b) Simulated SWE for individual tile components at the evaluation site (Figure 1). Top left uses model parameters introduced for the tiled model from Tuolumne, CA while the top right uses parameters from Jemez, NM (Table 3). c) Simulated daily streamflow values between the non-tiled and tiled model (with both the Tuolumne and Jemez parameters) compare to observed streamflow. d) The streamflow ratio between the tiled model and non-tiled model for both configuration of the tiled model in Chiwawa, WA.

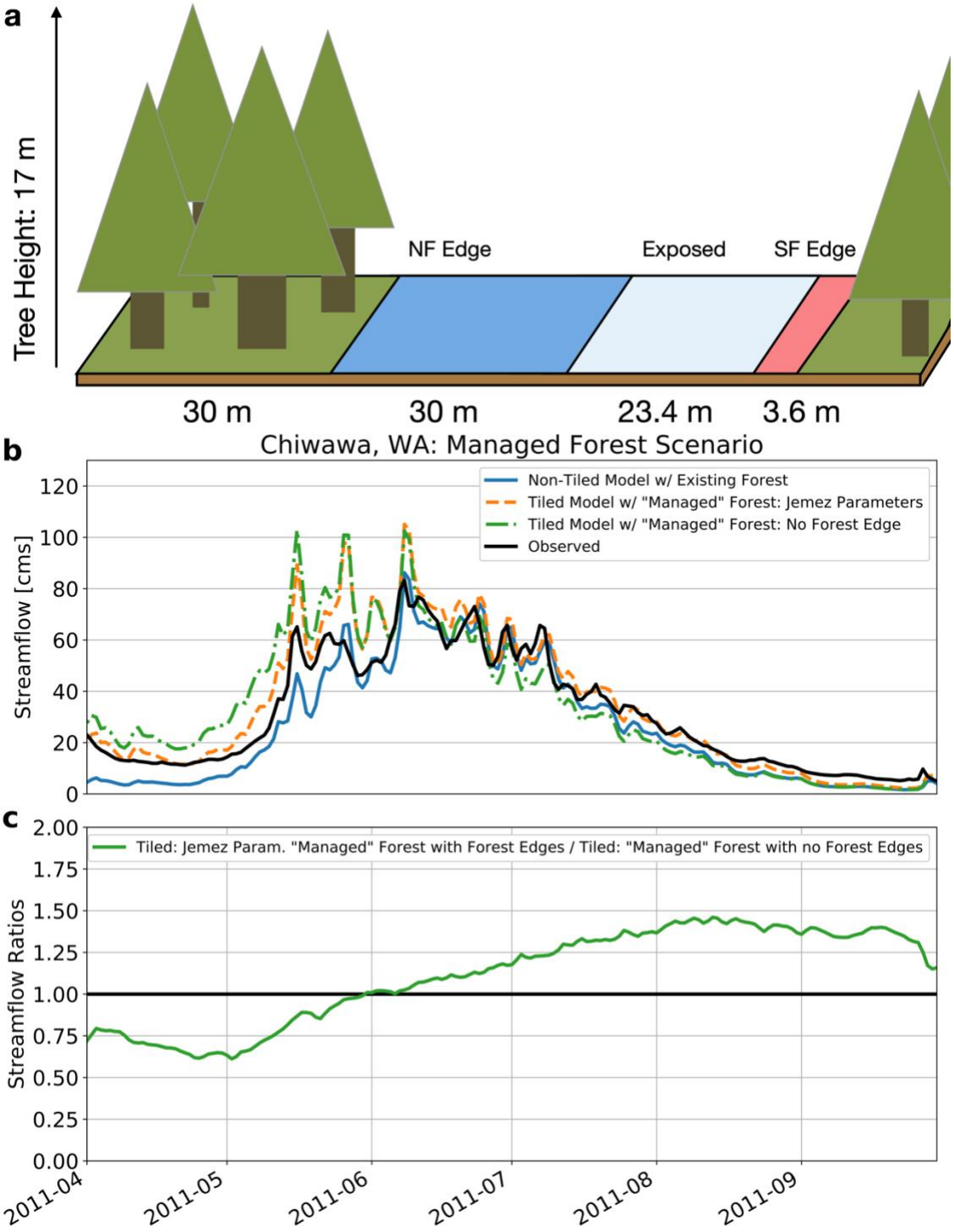

Figure 10: a) Conceptual diagram of the forest management strategy within an individual tiled model grid cell. Note: the grid cell is not drawn to scale, exaggerated length wise. b) Simulated daily streamflow values with different model configurations compared to observed streamflow. Note: Tiled model with Tuolumne parameters is not shown dude to similarity in results to the tile

model with Jemez parameters. c) Streamflow ratio between tiled model with a managed forest and the tiled model without forest edges and a managed forest.